Mechanical Systems and Signal Processing 211 (2024) 111241

Contents lists available at ScienceDirect

Mechanical Systems and Signal Processing

journal homepage: www.elsevier.com/locate/ymssp

Simultaneous low-frequency vibration suppression and energy harvesting using a metastructure with alternately combined nonlinear local resonators

Che Xu [a], Yaowen Yang [b], Chun H. Wang [a], Liya Zhao [a,*]

[a] School of Mechanical and Manufacturing Engineering, University of New South Wales, Sydney 2052 NSW, Australia
[b] School of Civil and Environmental Engineering, Nanyang Technological University Singapore, 50 Nanyang Ave, Singapore 639798, Singapore

ARTICLE INFO

Communicated by Daniil Yurchenko

Keywords:
Mechanical metastructure
Energy harvesting
Vibration suppression
Local resonators
Bistable oscillator
Piezoelectric devices

ABSTRACT

This paper proposes a novel dual-functional nonlinear metastructure for amplitude-robust simultaneous vibration suppression and energy harvesting, consisting of combined bistable and monostable cubic-hardening nonlinear electromechanical resonators that are alternately arranged on a host structure. The proposed design can effectively achieve wide bandgap even at high acceleration levels, suppress the undesired resonance transmission peaks outside the bandgap that are deemed as inevitable troubles in conventional linear metastructures, and generate power across a broad bandwidth at low frequencies. It is shown experimentally that the fabricated nonlinear prototype suppresses the unwanted resonance peaks by up to 70.5% while widening the bandgap by 52%, compared to the linear counterpart. A distributed-parameter electromechanically coupled model is established to verify the experimental measurements. Analytical expressions for the dynamic and electrical responses are explicitly derived using the harmonic balance method, based on which the interplay between several key parameters and their influences on the performance of the system are investigated, including the cubic nonlinear stiffness, mass ratio, load resistance, and electromechanical coupling strength. The findings provide a valuable guideline for accurately assessing the dual capabilities and facilitate efficient optimization of the next-generation nonlinear metastructure system.

1. Introduction

Locally resonant vibration suppression metastructures are finite structures assembled with periodically arranged local resonators on a host structure, achieving passive vibration suppression around the natural frequencies of these attached local resonating oscillators due to the out-of-phase motion between the primary structure and the oscillators. As a result, a stop-band is created that prevents vibration transmission in the primary structure [1,2]. The distributed local resonators can be considered as a superior alternative to the traditional low-degree-of-freedom absorber systems, as they allow for the discrete distribution of masses and require much less space. Moreover, they can be integrated into the primary structure during the fabrication process [3], thereby minimizing both post-installation and maintenance costs.

Conventional linear metastructures exhibit a very limited frequency band for effective vibration suppression. To enhance their

* Corresponding author.
E-mail address: liya.zhao2@unsw.edu.au (L. Zhao).

https://doi.org/10.1016/j.ymssp.2024.111241
Received 28 September 2023; Received in revised form 25 December 2023; Accepted 7 February 2024
Available online 17 February 2024

performance, a feasible solution involves the incorporation of adaptive materials (e.g., piezoceramics, shape memory alloys, etc.) into the local resonators, thereby enabling their resonating frequencies to be altered by providing additional power and matching them with the environmental frequency [4–6]. Other frequency tuning approaches include imposing mechanical deformation [7] or varying the temperature of temperature-dependent moduli of specific materials [8]. However, these tuning techniques reply on exceedingly precise design and accurate fabrication, resulting in increased implementation complexity. Another commonly employed means to enhance the performance of conventional metastructures is by tailoring the natural frequencies of the local resonators. Alshaqaq and Erturk [9] proposed a piezoelectric metastructure where the shunt resonant frequencies of the local resonators follow a grading pattern, forming an increase in the vibration attenuation bandgap by 65 %. Hu [10] analytically investigated the effects of the frequency spacing and damping ratio on the attenuation bandgap characteristics of a graded metamaterial beam. Xiao et al. [11] studied the wave propagation with multiple periodic arrays on a local resonating metamaterial beam and achieved much broader bandgaps. Zhang et al. [12] applied the bistable feature of origami structures to both one-dimensional beam-like and two-dimensional plate-like metastructures. They numerically and experimentally studied the influence of the bistable origami units on the vibration isolation ability. Wu et al. [13] proposed a metamaterial beam featuring X-shaped local resonators, which achieved enhanced adjustability to form bandgaps at specific target frequencies through proper parametrical design. Hu et al. [14] enhanced the vibration suppression performance of a metastructure beam utilizing internally coupled local resonators. Cai et al. applied local resonators with compliant quasi-zero stiffness on metamaterial plates [15] and pipes [16], achieving ultra-low-frequency bandgaps. Integrating inerters into the local resonators is also a convenient way of enhancing the vibration suppression performance, which can potentially broaden the bandgap as well as reducing the lower frequency limit of the bandgap by increasing the effective mass ratio between the resonators and the primary structure. Related works include studies by Xiao et al. [17], Jamil et al. [18], and Aladwani et al. [19].

There have been other studies on enhancing the vibration suppression performance of metastructures by investigating the effect of structural nonlinearities. These studies involve employing monostable [20], bistable [21,22], or piecewise stiffness linearities [23]. Mosquera-Sánchez and De Marqui [20] studied the influence of negative capacitance-based cubic-type piezoelectric shunt circuits on the vibration absorption performance of a linear metastructure chain. Xia et al. [21,22] reported a metastructure with bistable mechanical oscillators, where the chaotic oscillations in the bistable oscillators suppressed the vibration of the primary structure in a wider range of amplitude-dependent bandwidth than the linear bandgap. Banerjee et al. [23] theoretically investigated a single impacting mass-in-mass unit cell as a metastructure building block, realizing vibration attenuation through the sub- and superharmonic and chaotic responses. Some other studies intended to find the optimized performance in nonlinear metastructures. Casalotti et al. [24] studied the multi-mode vibration absorption capability of nonlinear local resonators with cubic restoring forces attached to a metamaterial hinged-hinged beam, and achieved a significant reduction in the oscillation amplitudes of the first three modes through optimizing the constitutive parameters in the absorbers. Vasconcellos and Silveira [25] replaced one of the linear oscillators on a metastructure chain with a nonlinear one with hardening type stiffness, and found the optimal position and stiffness coefficients for optimizing the vibration suppression performance without increasing the total mass of a structure.

The kinetic energy localized within the oscillating local oscillators offers a viable natural energy source that can be utilized for small-scale power generation. It is thus possible to create a dual-functional metastructure that simultaneously accomplishes vibration suppression and energy harvesting. The dual functionality of the metastructure provides significant advantages in establishing self-powered Internet of Things (IoT) systems [26]. Traditional IoT systems require numerous sensors that are distributed throughout a monitored structure, which necessitates either cumbersome wired power supply or frequent batteries recharging or replacements. Integrating energy-transducing elements that harness the localized vibrational energy on the local oscillators will potentially eliminate the need for an external power supply. However, there appears to be a contradiction between energy harvesting and vibration suppression concerning the frequency bandwidth and vibration amplitude. Energy harvesting benefits from a broader bandwidth with high-amplitude vibration, whereas vibration suppression aims to reduce vibration amplitudes and narrow the frequency range with large vibrations. Dual-functional metastructures have been studied in several papers [9,14,27–32]. Sugino and Erturk [32] studied the performance of a metastructure beam with energy harvesting local resonators, showing that the vibration suppression capability remains largely unaffected while harvesting useful energy. Hu et al. [14,33] analytically studied the dual-functional metastructure with internally coupled oscillators. Bukhari and Barry [28] studied the bandgap structure of a nonlinear metastructure chain with linear electromechanical resonators and investigated the influence of different parameters of the resonators on the band structure. Hobeck and Inman [3] employed piezoelectric zigzag beams as power generating local absorbers to achieve low-frequency vibration suppression and energy harvesting. They showed that allowing an increase of 82 % increase in vibration amplitude of the host structure yielded a remarkable 1500 % increase in the total output power.

However, attaching distributed periodic local resonators to the host structure inevitably leads to the emergence of many undesired resonance peaks around the bandgap (i.e., target frequency region for vibration suppression), endangering the host structure if the external excitations are around these frequencies. In particular, for low-frequency vibration suppression, these unnecessary peaks are even more risky since their amplitudes can be large. Although incorporating nonlinearities in the metastructures is capable to mitigate the unwanted peaks, the vibration suppression bandwidth is highly amplitude-dependent. For example, while bistable local resonators help attenuate the unwanted peaks, the bandgap completely disappears at high acceleration levels [21,22]. Moreover, while nonlinear broadband energy harvesting has been widely investigated [34–38], the current state-of-the-art literature lacks comprehensive quantitative analysis on the complex trade-off behaviours between energy harvesting and vibration attenuation in a nonlinear metastructure. To address the above issues, in this paper, a novel dual-functional nonlinear metastructure is proposed and investigated for amplitude-robust simultaneous vibration suppression and energy harvesting, by incorporating combined bistable and monostable cubic-hardening nonlinearities in the oscillators that are alternately arranged. The proposed metastructure focuses on achieving wide bandgap even at high acceleration levels, suppressing the unwanted resonance transmission peaks, and generating power across a

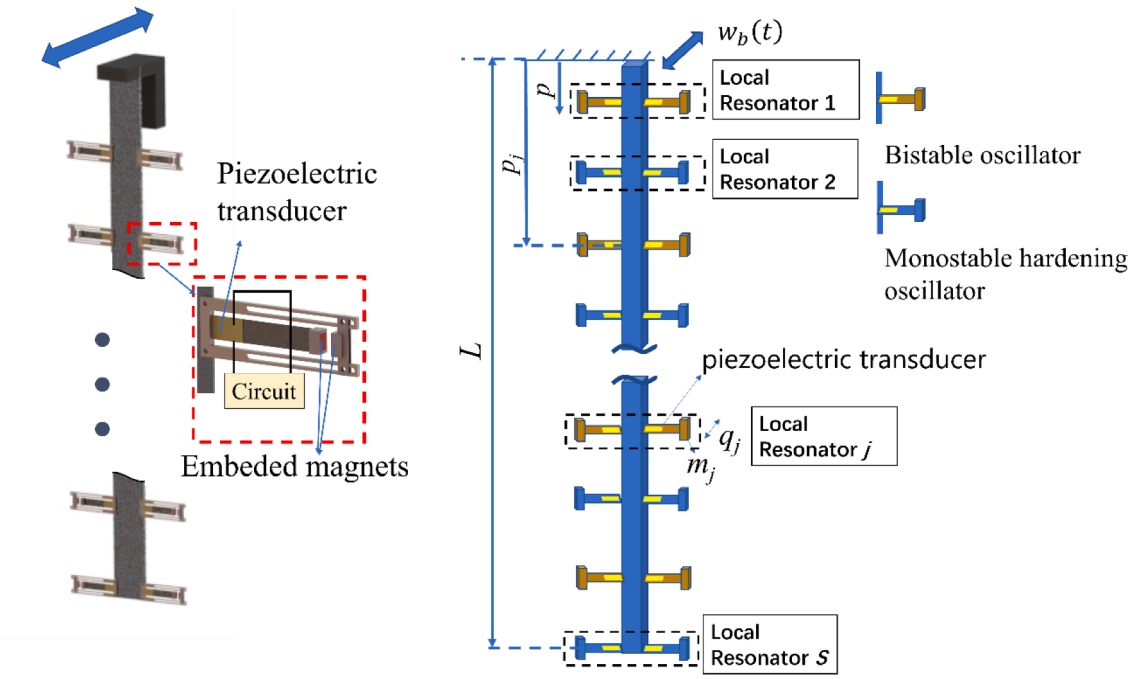

Fig. 1. Schematic of the proposed dual-functional nonlinear metastructure with alternate bistable and monostable cubic-hardening local resonators.

broad bandwidth specifically targeting low frequencies, e.g., below 20 Hz. In our previous research [39], we numerically demonstrated the benefits of the conceptual design using a lumped metastructure chain model and evaluated the dual functions with a perfection rate weighed index. In this paper, the experimental results obtained from a fabricated nonlinear metastructure prototype are validated using an established distributed-parameter electromechanically coupled model. Analytical expressions of the dynamic and electrical responses of the proposed nonlinear metastructure are explicitly derived based on the harmonic balance method, providing valuable insights and guidelines for accurately evaluating the well-balanced dual-capabilities of vibration suppression and energy harvesting, as well as enabling efficient system optimization. Moreover, this study examines the influences of the nonlinear stiffness, load resistance, and electromechanical coupling on the mechanical and electrical outputs, to provide a comprehensive understanding on the interplay between these parameters and how they collectively contribute to the overall performance of the system.

The rest of the paper is organized as follows. In section 2, the schematic of the proposed nonlinear metastructure is introduced. Its enhanced performance is experimentally demonstrated and then validated using a distributed-parameter electromechanically coupled model. The analytical solution derivation and validation are presented in section 3. Section 4 discusses the dynamics of the nonlinear metastructure. The influences of several key parameters, including the cubic nonlinear stiffness, mass ratio, load resistance, and electromechanical coupling strength, on the system performance are investigated in section 5. Section 6 concludes the findings of this work.

2. Experiment and electromechanically coupled modeling

The structure depicted in Fig. 1 outlines the proposed nonlinear metastructure, consisting of a primary cantilever beam and multiple pairs of piezoelectric oscillators to serve as the mechanical local resonators as well as the energy harvesters. Two types of stiffness nonlinearities, namely the bistable and monostable cubic-hardening nonlinearities, are arranged equidistantly and alternately along the length of the primary beam. An experimental prototype is fabricated with an aluminum primary beam and six pairs of aluminum oscillators, as shown in Fig. 2(a). The dimension of the primary beam is $850 \times 50 \times 3$ mm^3. The six pairs of oscillators are equidistantly positioned on the two sides of the primary beam. The cross-section of the oscillators is 20×0.5 mm^2. On each oscillator, a piezoelectric sheet (MFC M2807-P2 from Smart Materials Corp.) of $28 \times 7 \times 0.3$ mm^3 is attached to convert the vibration energy into electricity with its two electrodes connected across a load resistor, forming a simple AC energy harvesting interface circuit. The piezoelectric capacitance is 21.5nF. The stiffness nonlinearity is induced by repulsive magnetic dipoles. One magnet is attached to each oscillator's free end, while the other magnet is fixed onto the acrylic glass frame surrounding the oscillator. The frame has a thickness of 3 mm and is sufficiently high in its stiffness to be assumed a rigid structure. The experimental setup is shown in Fig. 2 (b).

By changing the distance d between the magnets, the linearized natural frequency and the nonlinear stiffness of the oscillators can be adjusted. When d exceeds a critical value d_{cr}, the oscillator is in a monostable cubic-hardening state with a single equilibrium position; whereas when d is below d_{cr}, the oscillator enters a bistable state with two symmetric equilibrium positions. During the experiment, a function generator (TENMA 72-3555) and power amplifier (APS 125) are connected to a long-stroke shaker (APS 113)

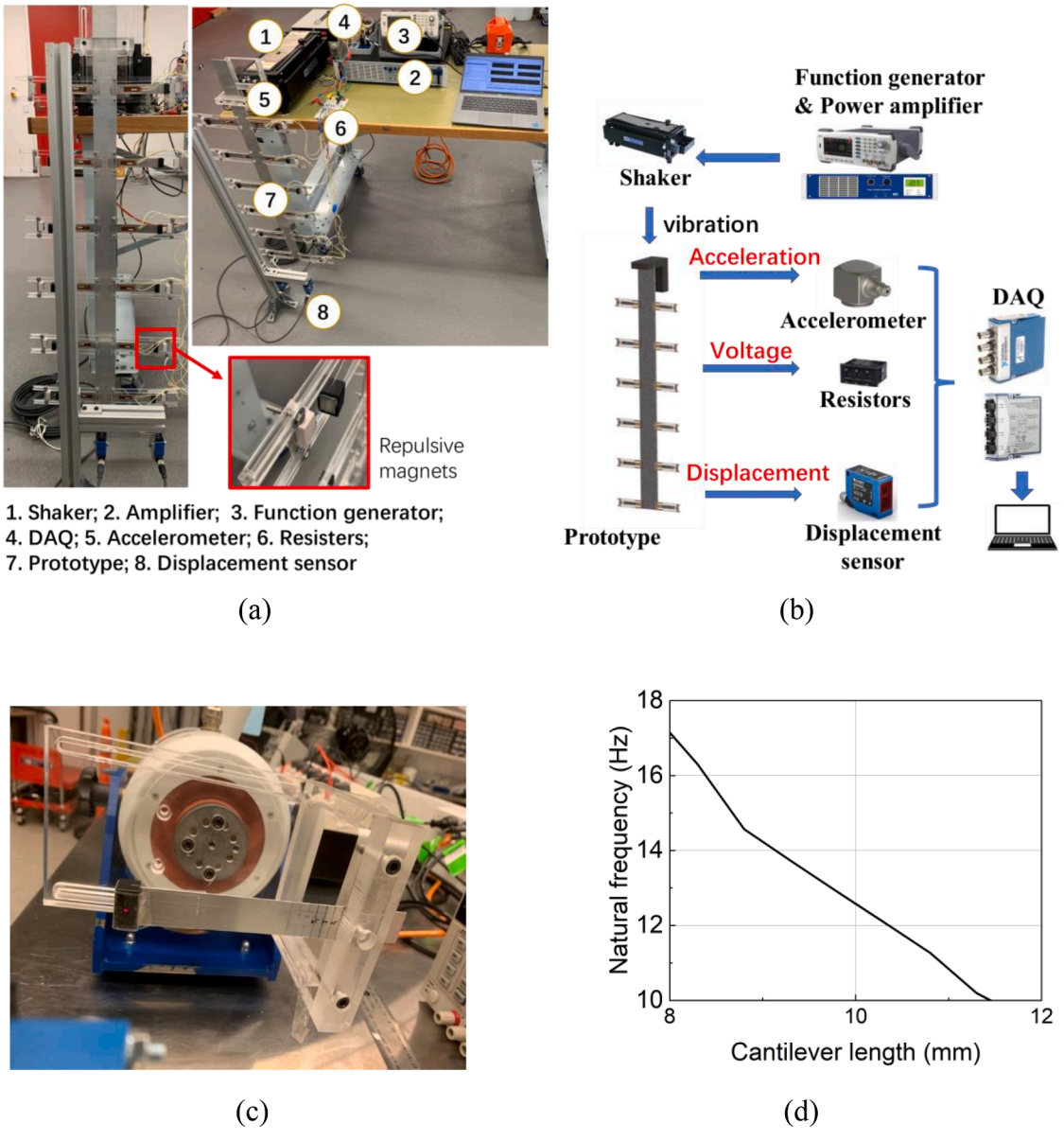

Fig. 2. (a) Experimental setup and (b) test procedure for the proposed nonlinear metastructure with alternately combined bistable and monostable cubic-hardening resonators. (c) Experimental setup and (d) measured variation of natural frequency with length of locally attached cantilever oscillator. Results are for linear local resonators.

that provides harmonic base vibratory excitation at the fixed end of the primary beam. Frequency upsweeping is conducted with the base acceleration level maintained constant at each frequency. The acceleration is monitored by an accelerometer and recorded through the NI9234 data acquisition module. Two displacement sensors (Wenglor CP24MHT80) are used to monitor the displacements of the oscillators and the primary beam. The voltage across the electrodes of the piezoelectric sheet is recorded by the NI9229 data acquisition module. The first three natural frequencies of the primary beam are predetermined as 2.9 Hz, 14.9 Hz, and 40.6 Hz, among which the second mode of 14.9 Hz is selected as the target frequency for low-frequency vibration suppression. The total tip mass at the free end of each resonator, including the magnet and its fastening frame is $M_{tip} = 6.4$ g. In the linear metastructure, the lengths of the linear local resonators are set to $L = 93.2$ mm, and the linearized natural frequencies of all oscillators are consistently 14 Hz. In the nonlinear metastructure, the linearized natural frequencies of the monostable cubic-hardening oscillators in the pre-buckled state and the intra-well resonant frequencies of the bistable oscillators in the post-buckled state are also uniformly set to 14 Hz by adjusting L and d. The natural frequency of the linear oscillator decreases with the increasing length L, as given in Fig. 2(d), measured through an experimental setup in Fig. 2(c). In the nonlinear oscillators, an equivalent negative linear stiffness is induced by the repulsive magnetic interaction, along with the positive cubic stiffness effect. Using a similar experimental setup in Fig. 2(c), L is firstly decreased in order

to increase the overall linear stiffness, thus the natural frequency becomes higher compared to the linear oscillator; subsequently, after applying the repulsive magnet, the distance d is adjusted to bring the linearized natural frequency back to the target one at 14 Hz. The specific parameters for the monostable and bistable cases are, respectively, $L = 7.90$ cm, $d = 15.4$ mm, and $L = 7.90$ cm, $d = 14.0$ mm. Following the assembly of the metastructure system, minor adjustments of L and d is further conducted to correct any errors in manufacturing and assembly. Here and hereafter, such a system consisting of local resonators with identical linearized frequencies is referred to as the *uniform* metastructure. Conversely, if the linearized frequencies of the local resonators are arranged to follow a specific pattern, the system is denoted as the *graded* metastructure. For example, in the experiment, the pattern is configured as [12 12.8 13.6 14.4 15.2 16] Hz. The load resistance is set to 510kΩ in all AC circuits connected to the energy harvesting oscillators.

The experimental results are further verified through direct comparison against a distributed-parameter electromechanically coupled model. A linear metastructure is considered first. The governing mechanical and electrical equations can be expressed as

$$EI\frac{\partial^4 w_{rel}(p,t)}{\partial p^4} + c_s I\frac{\partial^5 w_{rel}(p,t)}{\partial p^4 \partial t} + c_a\frac{\partial w_{rel}(p,t)}{\partial t} + m\frac{\partial^2 w_{rel}(p,t)}{\partial t^2} - \sum_{j=1}^{S}\left(k_{0,j}q_j + c_j\frac{dq_j}{dt} - F_{m,j} + \theta_j v_j\right)\delta(p-p_j) = -m\frac{d^2 w_b(t)}{dt^2} \tag{1}$$

$$m_j\frac{d^2 q_j}{dt^2} + c_j\frac{dq_j}{dt} + k_{0,j}q_j + \theta_j v_j = -m_j\left(\frac{\partial^2 w_{rel}(p_j,t)}{\partial t^2} + \frac{d^2 w_b(t)}{dt^2}\right) + F_{m,j} \tag{2}$$

$$C_{p,j}\frac{dv_j}{dt} + \frac{v_j}{R_{L,j}} - \theta_j\frac{dq_j}{dt} = 0 \tag{3}$$

where the subscript j denotes the jth resonator. $w_{rel}(p,t)$ is the relative displacement of the primary beam with respect to the base at the position coordinate p; q_j is the relative displacement of the local resonator with respect to the primary beam; $w_b(t) = f\cos(\Omega_b t)$ is the excitation displacement at $p = 0$, with the amplitude of f and frequency at Ω_b; E is the Young's modulus of the primary beam; I is the moment of inertia of the cross-section with respect to the neutral axis of the primary beam; c_s and c_a are the coefficients of strain rate damping and viscous damping, respectively; m is the mass density of the primary beam; S is the total number of the local resonators; $\delta(p)$ is the Dirac delta function; m_j, $k_{0,j}$ and c_j are the equivalent lumped mass, stiffness and damping of the jth local resonator, respectively, where m_j is approximated by $m_j = \frac{33}{140}m_{b,j} + m_{tip}$ [40], with $m_{b,j}$ and m_{tip} being the mass of the composite resonator beam and the proof mass at the tip, respectively, and $k_{0,j}$ is stiffness of the initially linear resonator, calculated by $k_{0,j} = m_j{\Omega_{0,j}}^2$ based on the experimentally measured natural frequency $\Omega_{0,j}$ of the initially linear jth resonator; and θ_j, $C_{p,j}$, v_j are the electromechanical coupling constant, capacitance, and voltage output of the piezoelectric transducer on the jth oscillator, respectively. It should be noted that each pair of oscillators in the prototype is regarded as a single local resonator in the theoretical model. The magnetic force $F_{m,j}$ applied on the jth resonator can be modelled by the dipole–dipole interaction theory. In this model, it is simplified by fitting the experimentally measured force–displacement data with a cubic polynomial, expressed as

$$F_{m,j} = k_{m1,j}q_j - k_{m3,j}{q_j}^3 \tag{4}$$

The relative displacement $w_{rel}(p,t)$ of the primary beam can be represented by the superposition of eigenfunctions and generalized coordinates based on the expansion theorem, given by

$$w_{rel}(p,t) = \sum_{r=1}^{N}\phi_r(p)\eta_r(t) \tag{5}$$

where $\phi_r(p)$ is the rth eigenfunction, and $\eta_r(t)$ is the modal coordinate of the rth mode. Inserting Eqs. (4) and (5) into Eq. (1), multiplying it with $\phi_s(p)$ and integrating it from $p = 0$ to L, then applying the mass-orthogonality condition for the eigenfunctions, the governing equation for the primary beam is expressed as

$$\ddot{\eta}_r + 2\zeta_r\omega_r\dot{\eta}_r + {\omega_r}^2\eta_r - \sum_{j=1}^{S}\left(k_{1,j}q_j + k_{3,j}{q_j}^3 + c_j\dot{q}_j + \theta_j v_j\right)\phi_r(p_j) = -\int_0^L \phi_r(p)m\ddot{w}_b dp, r = 1,2,\cdots,N \tag{6}$$

where $k_{1,j} = k_{0,j} - k_{m1,j}$ and $k_{3,j} = k_{m3,j}$, which are the equivalent linear and cubic stiffness of the jth local resonator; and ζ_r is the rth modal damping factor. The overdot denotes the derivative with respect to time t. Substituting Eqs. (4) and (5) into Eq. (2) yields

$$m_j\ddot{q}_j + c_j\dot{q}_j + k_{1,j}q_j + k_{3,j}{q_j}^3 + \theta_j v_j = -m_j\sum_{r=1}^{N}\phi_r(p_j)\ddot{\eta}_r - m_j\ddot{w}_b \tag{7}$$

Eqs. (3), (6) and (7) are further transformed to the state-space form and numerically solved in MATLAB.

The transmittance T is defined here to be the ratio of the root mean square (RMS) amplitude of the absolute displacement at the free end of the primary beam to the RMS exciation displacement amplitude, that is, $T = (w_{rel}(L,t) + w_b(t))_{RMS}/(w_b(t))_{RMS}$. The frequency

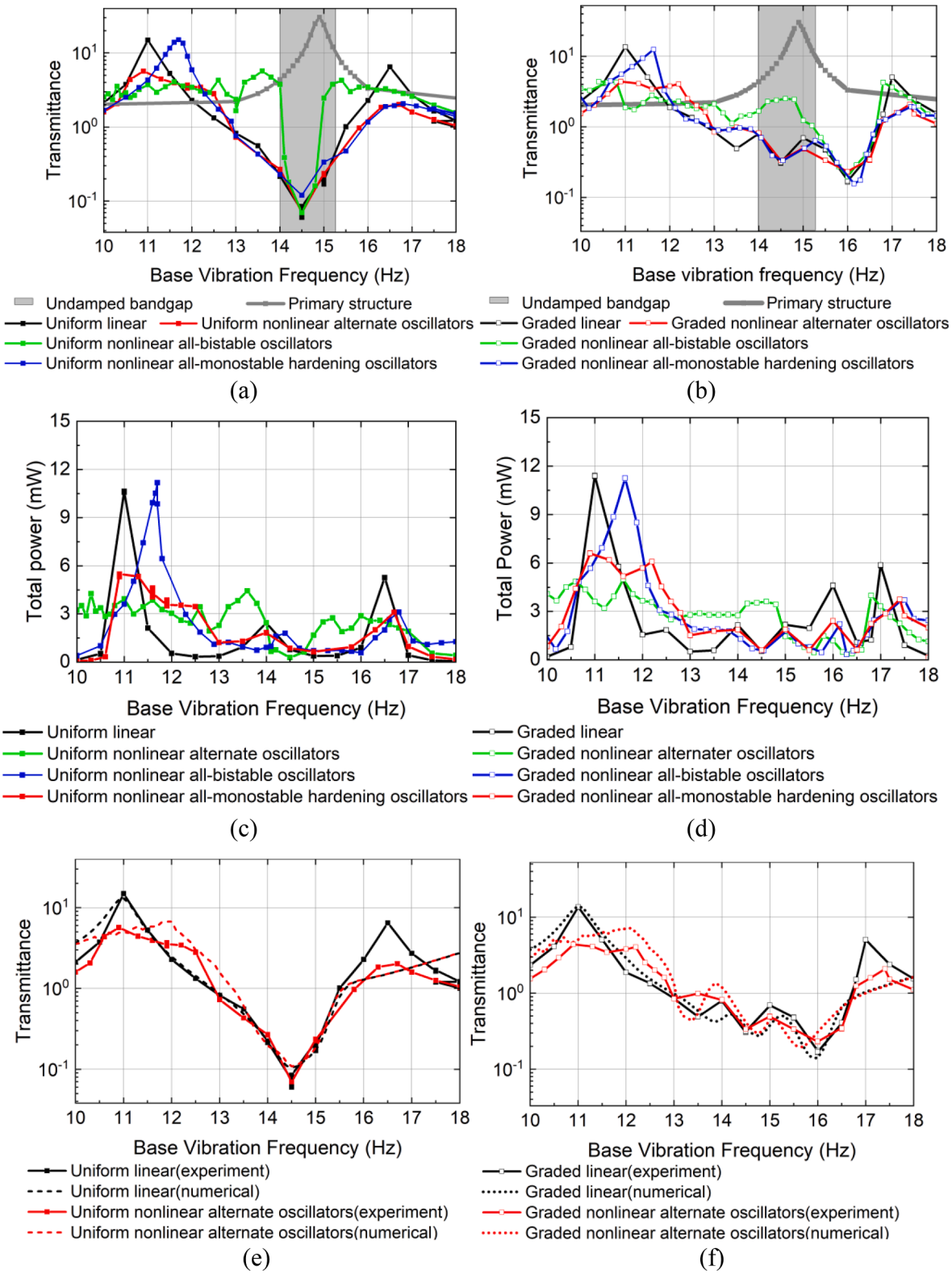

Fig. 3. Experimentally measured (a) (b) transmittance and (c) (d) total power output under an acceleration of 0.2 g: (a) (c) uniform and (b) (d) graded configuration. (e) (f) Distributed-parameter model prediction: (e) uniform and (f) graded configuration.

Table 1
System parameters.

Parameters of the host beam	
Density,ρ	2700 kg/m^3
Adjusted density,ρ_a	4000 kg/m^3
Beam Length, L	0.85 m
Beam Width, b	50×10^{-3} m
Beam Thickness, h	3×10^{-3} m
Adjusted Thickness,h_a	2.8×10^{-3} m
Modal damping ratios ζ_r ($r = 1 \sim 3$)	0.02, 0.03, 0.05
Young's modulus	69 GPa
Number of modes in expansion	3
Parameters of the local oscillators	
Proof mass at the tip m_{tip}	6.4×10^{-3} kg
Resonator width,b_j	20×10^{-3} m
Resonator thickness,h_j	0.5×10^{-3} m
Resonator damping c_j	0.02 Ns/m
Equivalent linear stiffness $k_{1,j}$ (j = 1–6)	Uniform: [−26.99, 53.98, −26.99, 53.98, −26.99, 53.98] N/m Graded: [−19.83, 45.13, −25.47, 57.11, −31.82, 70.50] N/m
Number of attachments	6 pairs
Cubic stiffness, $k_{3,j}$ (j = 1–6)	Uniform: [3.24, 1.08, 3.24, 1.08, 3.24, 1.08] $\times 10^5$N/m^3 Graded: [3.17, 0.79, 3.17, 0.79, 3.17, 0.79] $\times 10^5$N/m^3
Electrical-mechanical coupling parameters	
Capacitance,$C_{p,j}$	21.5nF
Load resistance,$R_{L,j}$	510,000 Ω
electromechanical coupling constant,θ_j	1.4667×10^{-4}N/V

range where $T < 1$ is referred to as the transmission bandgap. Fig. 3(a) shows the experimentally measured transmittance response of the fabricated nonlinear metastructure prototype with the uniform configuration at a constant base acceleration of 0.2 g, where the bistable and monostable cubic-hardening oscillators are alternately arranged, and the linearized natural frequencies (intra-well resonant frequencies in the bistable case) are uniformly tuned to 14 Hz. For comparison, the results for the linear metastructure, and the nonlinear metastructures with all bistable oscillators and all monostable oscillators are also included. The shaded area is the transmission bandgap for an infinitely long and undamped linear metastructure, calculated by $\Omega_j < \Omega_b < \Omega_j\sqrt{1+\mu}$ [2,41], where $\Omega_j = 14$ Hz is the linearized natural frequency of the oscillators and $\mu = 0.188$ is the mass ratio of the oscillators to the primary structure.

It is seen that with the linear metastructure, a transmission bandgap is successfully formed around the target second mode of the primary beam, from 12.9 to 15.4 Hz. However, like all traditional vibration absorber techniques, the addition of the distributed local resonators introduces two unwanted resonance peaks on the two sides of the bandgap. The effectiveness of the proposed nonlinear metastructure with an alternate arrangement is evident in significantly attenuating these undesirable peaks. On the other hand, the counterpart utilizing all bistable oscillators also allows for peak attenuation, but it induces a substantial narrowing of the transmission bandgap. Meanwhile, in the case of the counterpart employing all monostable cubic-hardening oscillators, although the bandgap is preserved, the adjacent left resonance peak experiences an undesirable increase. It is apparent that the alternate design outperforms these counterparts with a superior well-balanced performance in attenuating the unwanted resonance peaks as well as maintaining the transmission bandgap by combinedly incorporating the bistable intrawell and monostable periodic oscillations along with the bistable interwell chaotic oscillations. The graded configuration further broadens the transmission bandgap, as shown in Fig. 3(b), while preserving the peak attenuation outside the bandgap. Compared to the linear metastructure, the proposed nonlinear metastructure with graded configuration suppresses the left resonance peak by 70.5 % and the right peak by 61.9 % while widening the bandgap by 52 %. The average power generated from each local resonator is calculated through $P_j = {v_{RMS,j}}^2/R_{L,j}$, where $v_{RMS,j}$ is root mean square voltage across $R_{L,j}$. The total power output combinedly from the six pairs of oscillators is shown in Fig. 3(c) and 3(d). As shown in Fig. 3(c), at the power level of 2.5mW, the power bandwidth enhancement is 53.3 % and 37.5 % over the linear counterpart for the uniform and graded alternate configurations, respectively, At the power level of 3.5mW, for the uniform configuration, the alternate, all-bistable, and all-monostable designs widen the power bandwidth by 54.6 %, 18.2 %, and 9.1 %, respectively, compared to the linear counterpart. In the case of the graded configuration, the power bandwidth enhancement is 28.8 %, 22.2 %, and 11.1 % over the linear counterpart for the alternate, all-bistable, and all-monostable designs, respectively. In both configurations, the alternate design shows the highest percentage increase.

Comparison between the experimental measurements and theoretical predictions from the established distributed-parameter electromechanical model is presented in Fig. 3(e) and 3(f). The applied material parameters in simulation are given in Table 1. It is worth mentioning that the simulation adjusts the thickness and density of the beam to account for factors such as the added frames, cut holes, and other elements introduced during the process of establishing the testing system. The transmittance response as a function of the excitation frequency and the performance of vibration suppression, including the range of the unwanted resonance peak attenuation and transmission bandgaps, are well predicted.

Fig. 4(a) and 4(b) present the experimentally measured time-domain displacement responses of the nonlinear alternate

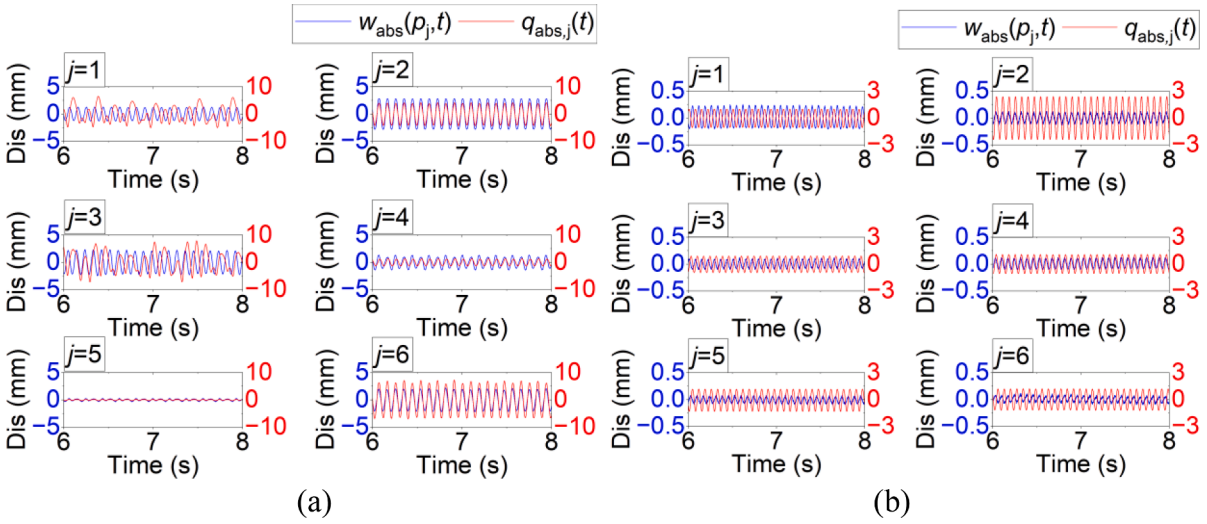

Fig. 4. Experimentally measured displacement time histories of the primary beam and the local resonators for the uniform configuration at the frequency of (a) 10.7 Hz and (b) 14 Hz, $w_{abs}(p_j,t)$ is the absolute displacement of the primary beam at the jth cell's position coordinate p_j; $q_{abs,j}(t)$ is the absolute displacement of the jth local resonator. The responses of $q_{abs,j}$ in (a) and (b) are adjusted to be relative to the equilibrium positions.

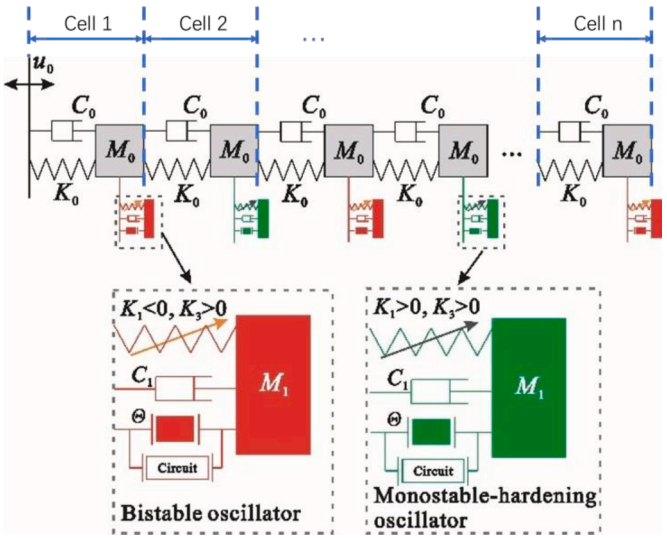

Fig. 5. Modelling of the proposed nonlinear alternate metastructure.

metastructure with uniform oscillators at the frequency of 10.7 Hz and 14 Hz, respectively. At the frequency of 14 Hz (Fig. 4(b)) within the transmission bandgap, most of the oscillators undergo either fully ($j = 1$ and 6) or partially ($j = 3$ and 5) out-of-phase oscillations with the primary beam, leading to a suppression of vibration in the primary beam. In such a case, the vibration cannot transmit through the primary structure. The responses at 10.7 Hz (Fig. 4(a)), which are around the left resonance peak outside the bandgap, reveal the emergence of inter-well chaotic vibrations in the 1st and 3rd oscillators. It results in nearly out-of-phase vibrations occurring intermittently between the oscillators and the primary structure. Consequently, even though the three monostable cubic-hardening oscillators ($j = 2$, 4 and 6) undergo in-phase oscillations with the primary structure, the vibration of the primary structure is still effectively suppressed, leading to the successful vibration attenuation around this unwanted resonance peak.

3. Harmonic balance analysis

To establish quantitative guidelines for accurately evaluating the relationship between vibration suppression and energy harvesting of the proposed nonlinear metastructure, as well as to gain a comprehensive understanding on the interplay between key parameters to facilitate efficient system design and optimization, in this section, the theoretical solution is derived based on a lumped-parameter

nonlinear metastructure chain, as shown in Fig. 5, and subsequently validated through numerical simulation. While the lumped-parameter model does not offer an exact quantitative description of the built experimental prototype given in Section 2, it is capable of capturing the overall characteristics of both vibration suppression and energy harvesting behaviours. Moreover, it provides a broader theoretical framework for analyzing the behaviour of similar nonlinear structures, extending beyond the existing prototypes and encompassing potential new designs as well. The nonlinear metastructure chain is modeled as a series connection of n cells. Each cell comprises a linear primary structure element including a primary mass M_0 supported by a linear spring K_0, along with a nonlinear local resonator consisting of a secondary mass M_1 supported by a nonlinear spring with coefficients K_1 and K_3. The associated mechanical damping terms are C_0 and C_1. The governing mechanical and electrical equations are rewritten in the lumped-parameter form, given by

$$\begin{cases} M_0\ddot{x}_i + C_0\left(2\dot{x}_i - \dot{x}_{i-1} - \dot{x}_{i+1}\right) + K_0(2x_i - x_{i-1} - x_{i+1}) - \Theta V_i \\ +C_1\left(\dot{x}_i - \dot{v}_i\right) + K_{1i}(x_i - v_i) + K_{3i}(x_i - v_i)^3 = 0, (i = 1, 2, \cdots, n-1) \\ M_0\ddot{x}_i + C_0\left(\dot{x}_i - x_{i-1}\right) + K_0(x_i - x_{i-1}) - \Theta V_i \\ +C_1\left(\dot{x}_i - \dot{v}_i\right) + K_{1i}(x_i - v_i) + K_{3i}(x_i - v_i)^3 = 0, (i = n) \\ M_1\ddot{v}_i + C_1\left(\dot{v}_i - \dot{x}_i\right) + K_{1i}(v_i - x_i) + K_{3i}(v_i - x_i)^3 + \Theta V_i = 0 (i = 1, 2, \cdots, n) \\ C_p\dot{V}_i + \dfrac{V_i}{R_L} - \Theta\left(\dot{v}_i - \dot{x}_i\right) = 0 (i = 1, 2, \cdots, n) \end{cases} \tag{9}$$

where x_i and v_i are the absolute displacements of M_0 and M_1 in the ith cell, respectively; x_0 is the base vibration displacement, which is expressed as $x_0 = f\cos(\Omega_b t)$ with f being the displacement amplitude and Ω_b the base excitation frequency; Θ, C_p, and R_L are the electromechanical coupling constant, piezoelectric capacitance, and load resistance in the AC energy extraction circuit, respectively, which are assumed to remain uniform across all resonators for the sake of simplicity; and the overdot represents differentiation with respect to time. The nonlinear elastic restoring force between M_0 and M_1 in the ith cell is $K_{1i}(v_i - x_i) + K_{3i}(v_i - x_i)^3$. The bistable and monostable cubic-hardening nonlinearities follow an alternating pattern, with $K_{1i} < 0$ for the bistable case, and $K_{1i} > 0$ for the monostable cubic-hardening case. Introducing the relative displacement $y_i = v_i - x_i$, Eq. (9) becomes

$$\begin{cases} M_0\ddot{x}_i + C_0\left(2\dot{x}_i - \dot{x}_{i-1} - \dot{x}_{i+1}\right) + K_0(2x_i - x_{i-1} - x_{i+1}) - \Theta V_i \\ -C_{1i}\dot{y}_i - K_{1i}y_i - K_{3i}y_i^3 = 0, (i = 1, 2, \cdots, n-1) \\ M_0\ddot{x}_i + C_0\left(\dot{x}_i - \dot{x}_{i-1}\right) + K_0(x_i - x_{i-1}) - C_1\dot{y}_i - K_{1i}y_i - K_{3i}y_i^3 - \Theta V_i = 0, (i = n) \\ M_1\left(\ddot{x}_i + \ddot{y}_i\right) + C_1\dot{y}_i + K_{1i}y_i + K_{3i}y_i^3 + \Theta V_i = 0, (i = 1, 2, \cdots, n) \\ C_p\dot{V}_i + \dfrac{V_i}{R_L} - \Theta\dot{y}_i = 0, (i = 1, 2, \cdots, n) \end{cases} \tag{10}$$

Equation (10) is further transformed into a dimensionless form in Eq. (11), where the dimensionless parameters are defined as follows. $\widehat{x}_i = \frac{x_i}{h}, \widehat{y}_i = \frac{y_i}{h}, \widehat{V}_i = \frac{C_p}{\Theta h}V_i, \Omega_0 = \sqrt{\frac{K_0}{M_0}}, \mu = \frac{M_1}{M_0}, \zeta_0 = \frac{C_0}{2M_0\Omega_0}, \zeta_1 = \frac{C_1}{2M_1\Omega_1}, h = \sqrt{\frac{K_0}{K_{31}}}, \omega_b = \frac{\Omega_b}{\Omega_0}, r_L = R_L C_p \Omega_0, z = \frac{f}{h}, k_e = \frac{\Theta^2}{C_p K_0}, k_{1i} = \frac{K_{1i}}{K_0}, k_{3i} = \frac{K_{3i}h^2}{K_0}, \tau = \Omega_0 t, \widehat{P}_i = \frac{{V_{RMS,i}}^2}{R_L K_0 \Omega_0 h^2}$, and the total power is given as $\widehat{P}_{total} = \sum_{i=1}^{n} \frac{\left(V_{RMS,i}\right)^2}{R_L K_0 \Omega_0 h^2}$.

$$\begin{cases} \widehat{x}_i'' + 2\zeta_0\left(2\widehat{x}_i' - \widehat{x}_{i+1}' - \widehat{x}_{i-1}'\right) + 2\widehat{x}_i - \widehat{x}_{i+1} - \widehat{x}_{i-1} \\ -2\mu\omega_i\zeta_1\widehat{y}_i' - k_{1i}\widehat{y}_i - k_{3i}\widehat{y}_i^3 - k_e\widehat{V}_i = 0 (i = 1, 2, \cdots, n-1) \\ \widehat{x}_i'' + 2\zeta_0\left(\widehat{x}_i' - \widehat{x}_{i-1}'\right) + \widehat{x}_i - \widehat{x}_{i-1} - 2\mu\omega_i\zeta_1\widehat{y}_i' - k_{1i}\widehat{y}_i - k_{3i}\widehat{y}_i^3 - k_e\widehat{V}_i = 0 (i = n) \\ \mu\left(\widehat{x}_i'' + \widehat{y}_i''\right) + 2\mu\omega_i\zeta_1\widehat{y}_i' + k_{1i}\widehat{y}_i + k_{3i}\widehat{y}_i^3 + k_e\widehat{V}_i = 0 (i = 1, 2, \cdots, n) \\ \widehat{V}_i' + \dfrac{\widehat{V}_i}{r_L} - \widehat{y}_i' = 0 (i = 1, 2, \cdots, n) \end{cases} \tag{11}$$

The dimensionless base excitation is thus $\widehat{x}_0 = z\cos(\omega_b\tau)$. The prime mark denotes the differentiation with respect to the dimensionless time τ. ω_i is the linearized natural frequency of the ith local resonator, where for monostable cubic-hardening case, $\omega_i = \sqrt{k_{1i}/\mu}$ ($k_{1i} >$

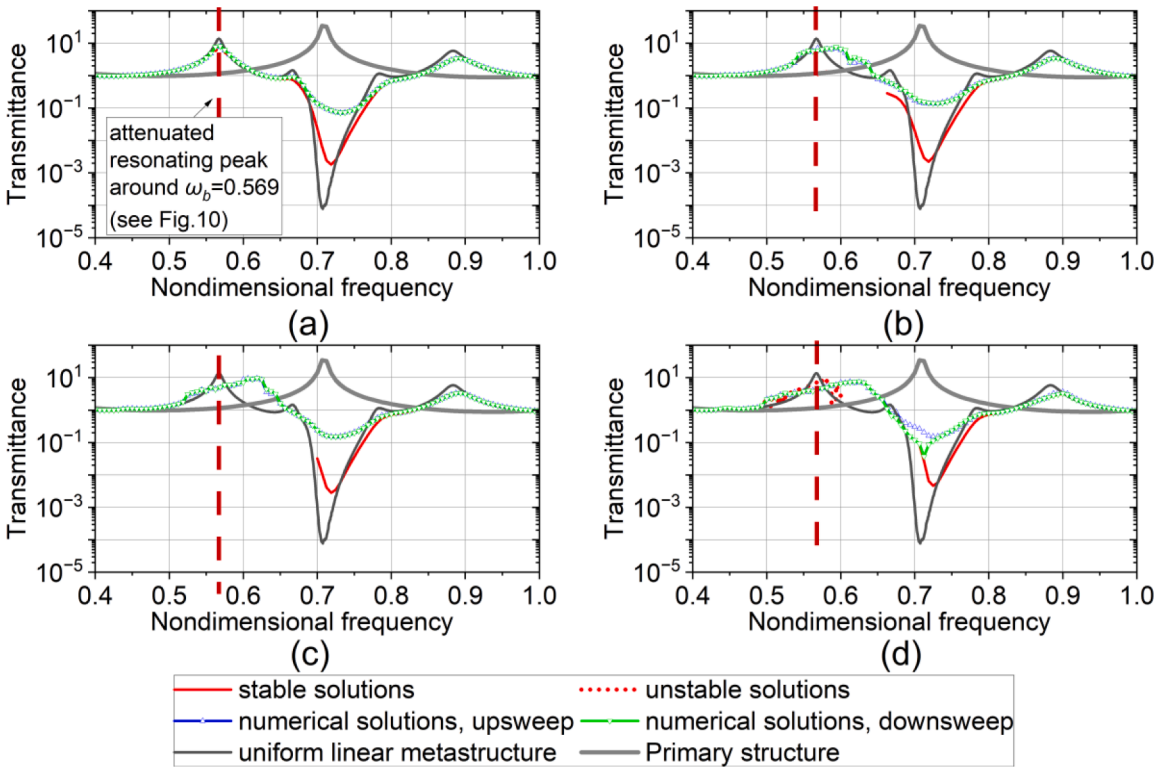

Fig. 6. Theoretical transmittance responses of the proposed metastructure (uniform configuration) with alternate nonlinear oscillators at A = (a) 0.0010, (b) 0.0030, (c) 0.0049, and (d) 0.0069.

0), while for the bistable case, $\omega_i = \sqrt{-2k_{1i}/\mu}$ ($k_{1i} < 0$). $\widehat{P}_i$ is the average power output from the ith cell. The steady-state responses of $\widehat{x}_i$, $\widehat{y}_i$ and $\widehat{V}_i$ are derived using the harmonic balance method, where they are assumed to be modeled by a truncated Fourier series, given by

$$\begin{cases} \widehat{x}_i = a_{1i}(\tau)\cos\omega_b\tau + b_{1i}(\tau)\sin\omega_b\tau + d_{1i}(\tau) \\ \widehat{y}_i = a_{2i}(\tau)\cos\omega_b\tau + b_{2i}(\tau)\sin\omega_b\tau + d_{2i}(\tau) \\ \widehat{V}_i = a_{3i}(\tau)\cos\omega_b\tau + b_{3i}(\tau)\sin\omega_b\tau \end{cases} \tag{12}$$

Taking the first derivative of Eq. (12) with respect to τ yields

$$\begin{cases} \widehat{x}_i' = \left(-\omega_b a_{1i} + b_{1i}'\right)\sin\omega_b\tau + \left(\omega_b b_{1i} + a_{1i}'\right)\cos\omega_b\tau + d_{1i}' \\ \widehat{y}_i' = \left(-\omega_b a_{2i} + b_{2i}'\right)\sin\omega_b\tau + \left(\omega_b b_{2i} + a_{2i}'\right)\cos\omega_b\tau + d_{2i}' \\ \widehat{V}_i' = \left(-\omega_b a_{3i} + b_{3i}'\right)\sin\omega_b\tau + \left(\omega_b b_{3i} + a_{3i}'\right)\cos\omega_b\tau \end{cases} \tag{13}$$

and the second derivative of $\widehat{x}_i$ and $\widehat{y}_i$ is

$$\begin{cases} \widehat{x}_i'' = \left(-\omega_b a_{1i}' - \omega_b^2 b_{1i}\right)\sin\omega_b\tau + \left(-\omega_b^2 a_{1i} + \omega_b b_{1i}'\right)\cos\omega_b\tau \\ \widehat{y}_i'' = \left(-\omega_b a_{2i}' - \omega_b^2 b_{2i}\right)\sin\omega_b\tau + \left(-\omega_b^2 a_{2i} + \omega_b b_{2i}'\right)\cos\omega_b\tau \end{cases} \tag{14}$$

Substituting the second and third equations in Eq. (12) and the third equation in Eq. (13) into the fourth equation in Eq. (11), letting a_{2i}', b_{2i}', a_{3i}' and b_{3i}' equal zero (i.e., considering the steady-state condition), and balancing the terms multiplied by sin $(\omega_b\tau)$ and cos $(\omega_b\tau)$, a_{3i} and b_{3i} can be expressed in terms of a_{2i} and b_{2i}, given by

$$\begin{cases} a_{3i} = \dfrac{(\omega_b r_L)^2}{(\omega_b r_L)^2 + 1} a_{2i} + \dfrac{\omega_b r_L}{(\omega_b r_L)^2 + 1} b_{2i} \\ b_{3i} = -\dfrac{\omega_b r_L}{(\omega_b r_L)^2 + 1} a_{2i} + \dfrac{(\omega_b r_L)^2}{(\omega_b r_L)^2 + 1} b_{2i} \end{cases} \tag{15}$$

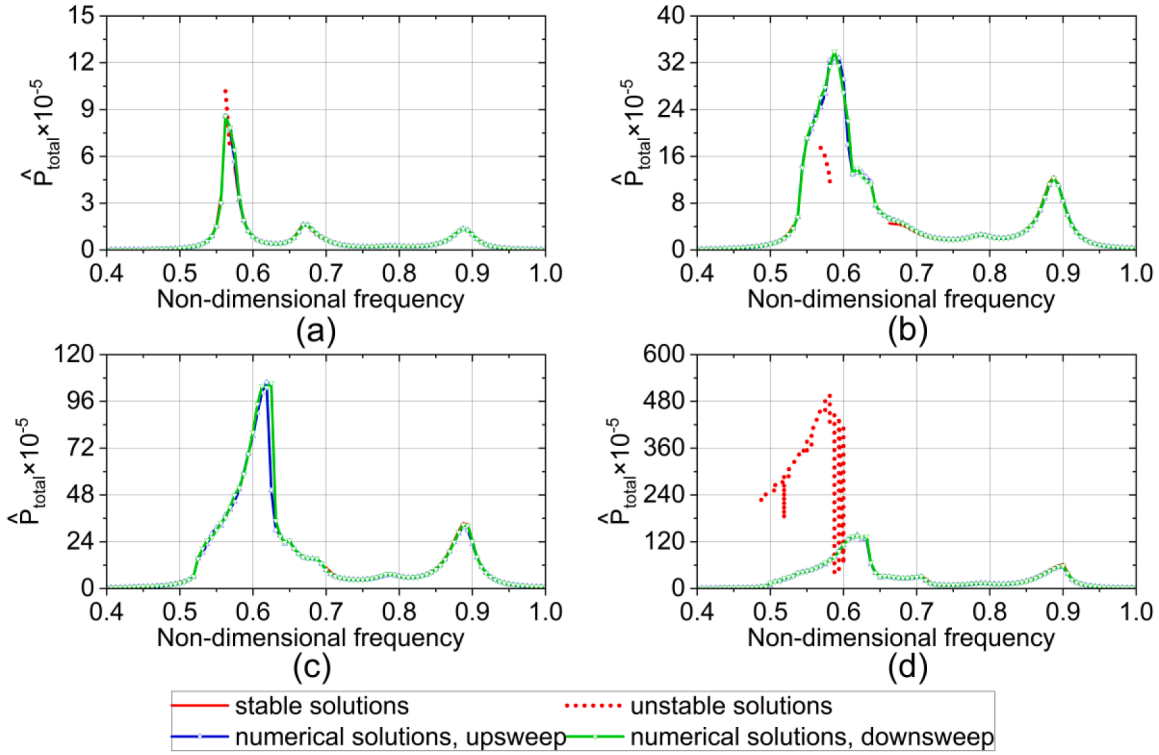

Fig. 7. Theoretical power output responses of the proposed metastructure (uniform configuration) with alternate nonlinear oscillators at A = (a) 0.0010, (b) 0.0030, (c) 0.0049, and (d) 0.0069.

Substituting Eqs. (12–15) into Eq. (11), letting $k_\theta = -\frac{(\omega_b r_L)^2 k_e}{(\omega_b r_L)^2+1}$, $c_\theta = \frac{r_L k_e}{(\omega_b r_L)^2+1}$, and balancing the terms multiplied by $\sin(\omega_b\tau)$, $\cos(\omega_b\tau)$ as well as the constant terms yield

$$\begin{cases} -\omega_b \boldsymbol{M}\boldsymbol{a}' + \boldsymbol{C}\boldsymbol{b}' + \left(\boldsymbol{K} + \boldsymbol{K}_\Theta - \omega_b{}^2\boldsymbol{M}\right)\boldsymbol{b} - \omega_b(\boldsymbol{C} - \boldsymbol{C}_\Theta)\boldsymbol{a} + \frac{1}{4}\boldsymbol{K}_3\left(3\boldsymbol{b}^3 + 3\boldsymbol{a}^{2\circ}\boldsymbol{b} + 12\boldsymbol{b}^\circ\boldsymbol{d}^2\right) = \boldsymbol{f}_1 \\ \omega_b \boldsymbol{M}\boldsymbol{b}' + \boldsymbol{C}\boldsymbol{a}' + \left(\boldsymbol{K} + \boldsymbol{K}_\Theta - \omega_b{}^2\boldsymbol{M}\right)\boldsymbol{a} + \omega_b(\boldsymbol{C} - \boldsymbol{C}_\Theta)\boldsymbol{b} + \frac{1}{4}\boldsymbol{K}_3\left(3\boldsymbol{a}^3 + 3\boldsymbol{b}^{2\circ}\boldsymbol{a} + 12\boldsymbol{a}^\circ\boldsymbol{d}^2\right) = \boldsymbol{f}_2 \\ \boldsymbol{C}\boldsymbol{d}' + \boldsymbol{K}\boldsymbol{d} + \frac{1}{4}\boldsymbol{K}_3\left(6\boldsymbol{b}^{2\circ}\boldsymbol{d} + 6\boldsymbol{a}^{2\circ}\boldsymbol{d} + 4\boldsymbol{d}^3\right) = 0 \end{cases} \tag{16}$$

where the matrices are expresses as follows, and the dimensions of the matrices are denoted by the subscripts.

$$\boldsymbol{K}_{2n\times 2n} = \begin{bmatrix} 2 & -k_{11} & -1 & 0 & 0 & & & & \\ 0 & k_{11} & 0 & 0 & 0 & & & & \\ -1 & 0 & 2 & -k_{12} & 1 & & & & \\ 0 & 0 & 0 & k_{12} & 0 & & & & \\ & & & & & \ddots & & & \\ & & & & & & -1 & 0 & 1 & -k_{1n} \\ & & & & & & 0 & 0 & 0 & k_{1n} \end{bmatrix}$$

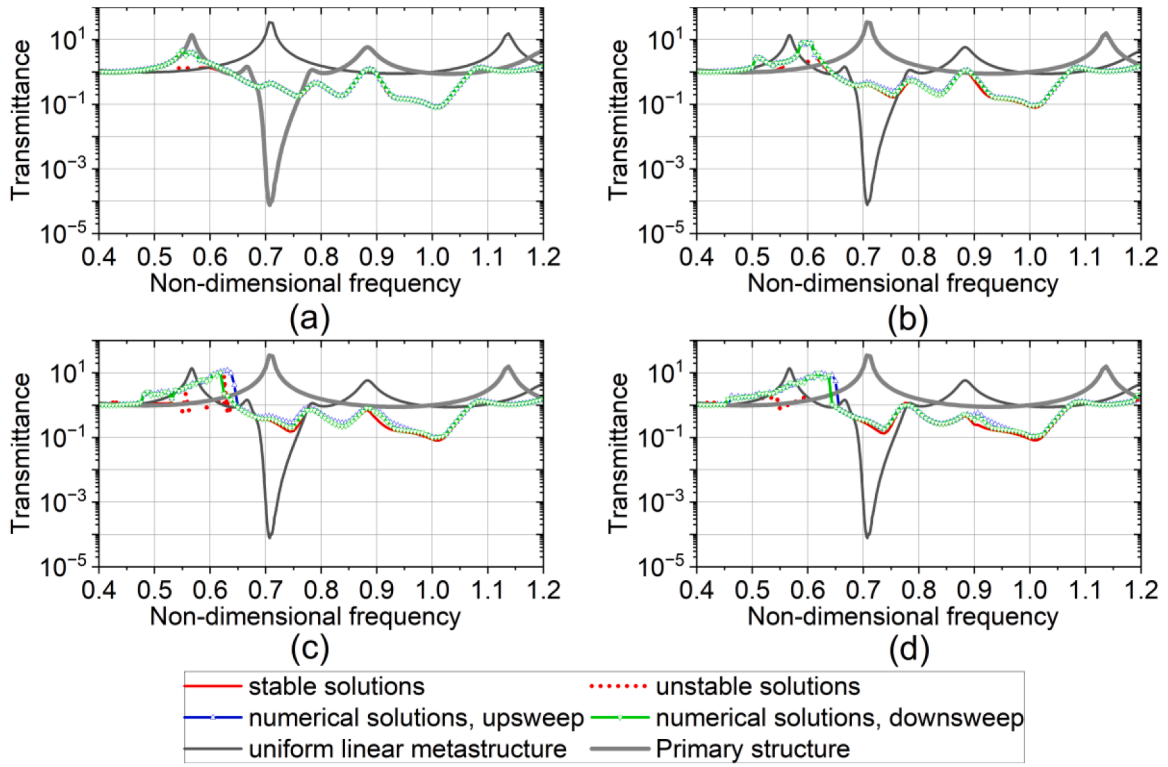

Fig. 8. Theoretical transmittance responses of the proposed metastructure (graded configuration, $\Delta = 0.1$) with alternate nonlinear oscillators at A = (a) 0.0009, (b) 0.0026, (c) 0.0044, and (d) 0.0061.

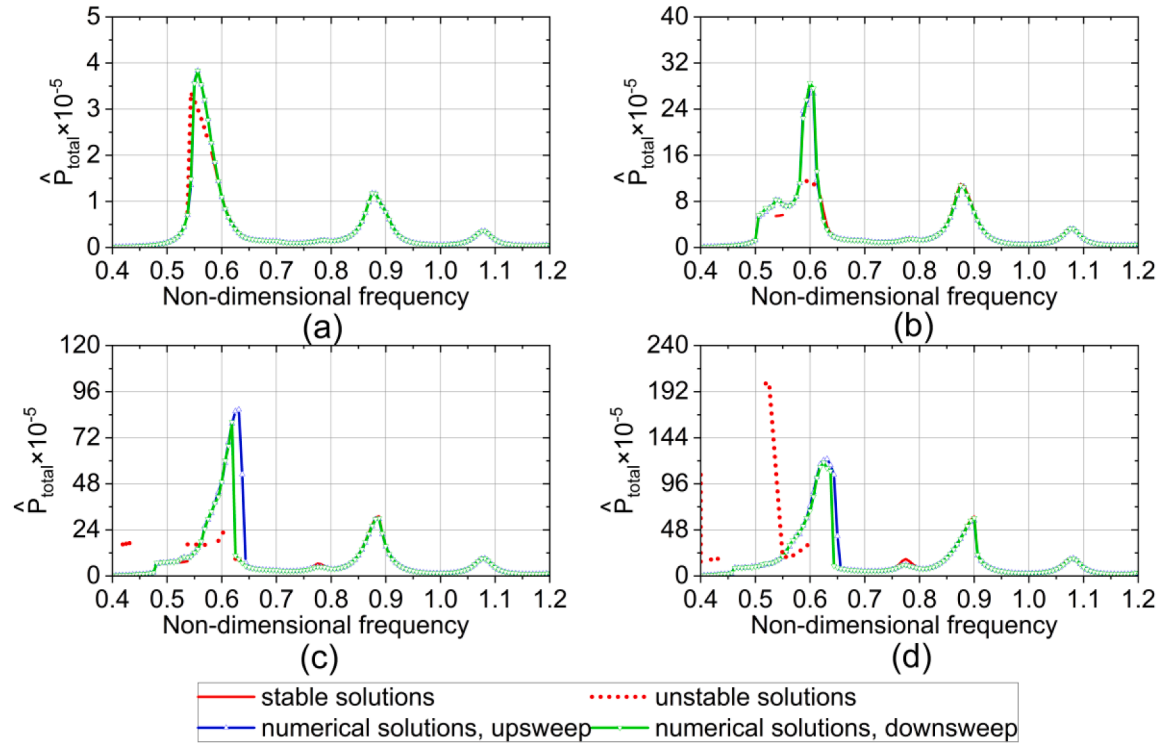

Fig. 9. Theoretical power output responses of the proposed metastructure (graded configuration, $\Delta = 0.1$) with alternate nonlinear oscillators at A = (a) 0.0009, (b) 0.0026, (c) 0.0044, and (d) 0.0061.

Table 2
System parameters.

Properties		Value
n		6
ζ_0, ζ_1		0.015, 0.01
μ		0.2
ω_i	Uniform	[0.706, 0.706, 0.706, 0.706, 0.706, 0.706]
	Graded	[0.625, 0.688, 0.756, 0.832, 0.915, 1.007]
h		0.1001 (Uniform), 0.1131 (Graded)
k_e		0.0056
r_L		1.081
k_{3i}		1 (i = 1–6)

$$\boldsymbol{C}_{2n\times 2n}=\begin{bmatrix} 4\zeta_0 & -2\mu\omega_1\zeta_1 & -2\zeta_0 & 0 & 0 & & & & \\ 0 & 2\mu\omega_1\zeta_1 & 0 & 0 & 0 & & & & \\ -2\zeta_0 & 0 & 4\zeta_0 & -2\mu\omega_2\zeta_1 & 2\zeta_0 & & & & \\ 0 & 0 & 0 & 2\mu\omega_2\zeta_1 & 0 & & & & \\ & & & & \ddots & & & & \\ & & & & & -2\zeta_0 & 0 & 2\zeta_0 & -2\mu\omega_n\zeta_1 \\ & & & & & 0 & 0 & 0 & 2\mu\omega_n\zeta_1 \end{bmatrix}$$

$$\boldsymbol{M}_{2n\times 2n}=\begin{bmatrix} m_1 & 0 & & & \\ m_2 & m_2 & & & \\ & & \ddots & & \\ & & & m_1 & 0 \\ & & & m_2 & m_2 \end{bmatrix},\boldsymbol{K}_{3,2n\times 2n}=\begin{bmatrix} 0 & -k_{31} & & & \\ 0 & k_{31} & & & \\ & & \ddots & & \\ & & & 0 & -k_{3n} \\ & & & 0 & k_{3n} \end{bmatrix}$$

$$\boldsymbol{K}_{\Theta,2n\times 2n}=\begin{bmatrix} 0 & k_\theta & & & \\ 0 & -k_\theta & & & \\ & & \ddots & & \\ & & & 0 & k_\theta \\ & & & 0 & -k_\theta \end{bmatrix},\boldsymbol{C}_{\Theta,2n\times 2n}=\begin{bmatrix} 0 & c_\theta & & & \\ 0 & -c_\theta & & & \\ & & \ddots & & \\ & & & 0 & c_\theta \\ & & & 0 & -c_\theta \end{bmatrix}$$

where $m_1 = 1$, $m_2 = \mu$, $\boldsymbol{a}_{2n\times 1}=[a_{11}\quad a_{21}\quad \cdots a_{1n}a_{2n}]^T$, $\boldsymbol{b}_{2n\times 1}=[b_{11}\quad b_{21}\quad \cdots b_{1n}b_{2n}]^T$, $\boldsymbol{d}_{2n\times 1}=[d_{11}\quad d_{21}\quad \cdots d_{1n}d_{2n}]^T$, $\boldsymbol{f}_{1,2n\times 1}=\begin{bmatrix}-\frac{2\zeta_0 A}{\omega_b} & 0 & \cdots & 0\end{bmatrix}^T$, and $\boldsymbol{f}_{2,2n\times 1}=\begin{bmatrix}\frac{A}{{\omega_b}^2} & 0 & \cdots & 0\end{bmatrix}^T$. The symbol '$\circ$' in Eq. (16) donates the Hadamard product of the matrices [42].

By setting $\boldsymbol{a}'$, $\boldsymbol{b}'$ and $\boldsymbol{d}'$ to zero, the steady-state solutions for the elements in $\boldsymbol{a}$, $\boldsymbol{b}$ and $\boldsymbol{d}$ can be obtained by numerically solving for the positive real solutions in MATLAB, yielding the steady-state frequency responses of $\widehat{x}_i$, $\widehat{y}_i$ and $\widehat{V}_i$ as given in Eq. (12).

The stability analysis is conducted based on the characteristics of the eigenvalues of the Jacobian matrix $\boldsymbol{J}$ at the solution $\boldsymbol{X} = \boldsymbol{X}_0$, which can be derived from Eq. (16) and expressed as

$$\boldsymbol{J}=\frac{\partial \boldsymbol{X}'}{\partial \boldsymbol{X}}=-\boldsymbol{A}^{-1}\left(\boldsymbol{B}+\frac{\partial \boldsymbol{D}}{\partial \boldsymbol{X}}\right)\text{ at }\boldsymbol{X}=\boldsymbol{X}_0\ (17)\text{where }\boldsymbol{X}=\begin{bmatrix}\boldsymbol{a}\\ \boldsymbol{b}\\ \boldsymbol{d}\end{bmatrix},\boldsymbol{A}=\begin{bmatrix}-\omega_b\boldsymbol{M} & \boldsymbol{C} & 0\\ \boldsymbol{C} & \omega_b\boldsymbol{M} & 0\\ 0 & 0 & \boldsymbol{C}\end{bmatrix},\boldsymbol{B}=\begin{bmatrix}-\omega_b(\boldsymbol{C}-\boldsymbol{C}_\Theta) & \boldsymbol{K}+\boldsymbol{K}_\Theta-{\omega_b}^2\boldsymbol{M} & 0\\ \boldsymbol{K}+\boldsymbol{K}_\Theta-{\omega_b}^2\boldsymbol{M} & \omega_b(\boldsymbol{C}-\boldsymbol{C}_\Theta) & 0\\ 0 & 0 & \boldsymbol{K}\end{bmatrix},$$

$$\boldsymbol{D}=\tfrac{1}{4}\boldsymbol{K}_3\begin{bmatrix}3\boldsymbol{b}^3+3\boldsymbol{a}^{2\circ}\boldsymbol{b}+12\boldsymbol{b}^\circ\boldsymbol{d}^2\\ 3\boldsymbol{a}^3+3\boldsymbol{b}^{2\circ}\boldsymbol{a}+12\boldsymbol{a}^\circ\boldsymbol{d}^2\\ 6\boldsymbol{b}^{2\circ}\boldsymbol{d}+6\boldsymbol{a}^{2\circ}\boldsymbol{d}+4\boldsymbol{d}^3\end{bmatrix}.$$

In Eq. (17), $\boldsymbol{X}_0$ can be determined as a stable solution if all real parts of the eigenvalues of $\boldsymbol{J}$ are negative. The transmittance T_r here is calculated as the ratio of the velocity amplitude of M_0 in the last cell at the free end (i.e., nth cell, Fig. 5) to the velocity amplitude of the base excitation at the fixed end. The analytical solutions are compared against the numerical simulations in Figs. 6–9. The employed system parameters are listed in Table 2.

The analytical solutions are validated for both the uniform and graded nonlinear metastructures through comparison with the numerical simulations. In the uniform metastructure case, the linearized natural frequencies ω_i for all the bistable and monostable cubic-hardening resonators are uniformly set to 0.706, which is around one of the resonance frequencies of the primary chain. The associated analytical and numerical results of the vibration transmittance are compared in Fig. 6, and the corresponding dimensionless power results are compared in Fig. 7. Four levels of base acceleration $A = z{\omega_b}^2$ at 0.0010, 0.0030, 0.0049, and 0.0069 are considered.

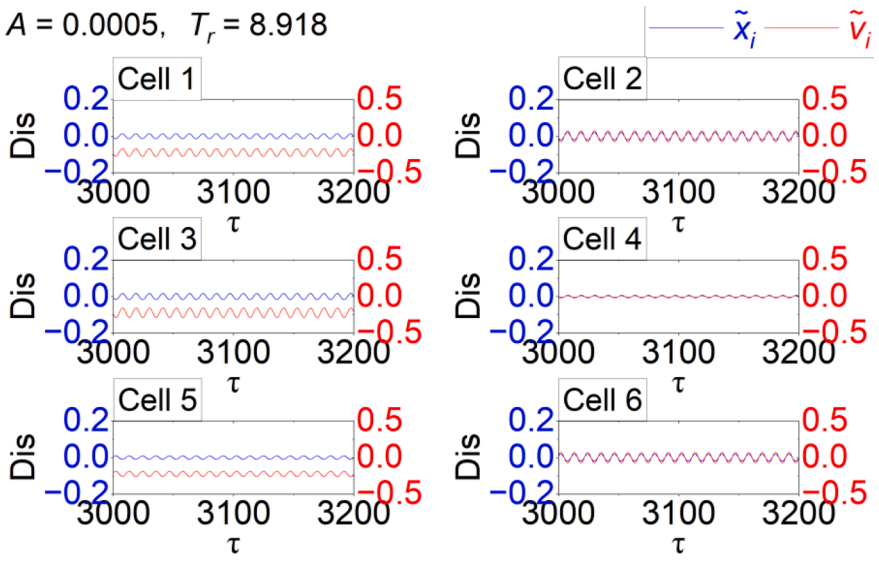

(a)

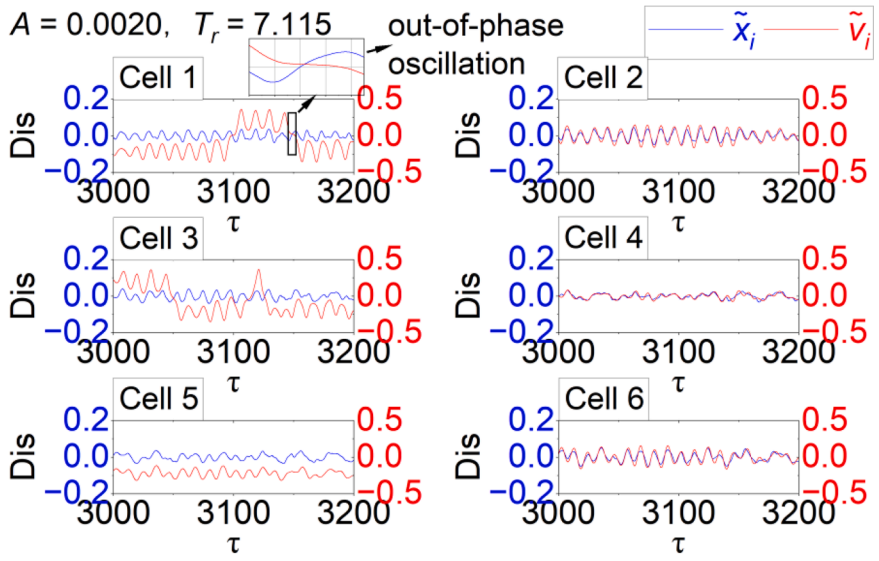

(b)

Fig. 10. Numerical time domain response of the primary structure (blue) and the local resonator (red) of each cell at $\omega_b = 0.569$ for the proposed metastructure (uniform) with alternate nonlinear oscillators at (a) $A = 0.0005$, (b) 0.0020, (c) 0.0049 and (d) 0.0089. Cell 1, 3, 5 are with bistable local resonators, cell 2, 4, 6 are with monostable cubic-hardening local resonators. (For interpretation of the references to colour in this figure legend, the reader is referred to the web version of this article.)

It is noticed that within a certain frequency range (e.g. $\omega_b = 0.54$–0.66 in Fig. 6(b) and 7(b)), the analytical solution is either unstable or unavailable. This occurs when one or more of the bistable resonators undergo inter-well chaotic oscillations, subsequently leading to chaotic oscillations in the monostable resonators as well as the primary chain, which is observed in numerical simulations and will be presented in Section 4. As shown in Fig. 6, the unwanted resonance peaks outside the bandgap are attenuated with the proposed nonlinear metastructure, with the percentage of the suppression as compared to the original linear peak amplitude increasing with the increase in the base acceleration. More importantly, at high accelerations (e.g., Fig. 6(d)), the proposed metastructure with alternately combined bistable and monostable cubic-hardening resonators successfully maintain a vibration transmission bandgap of comparable size to that of a uniform linear metastructure. This is in contrast to the metastructure with all bistable attachments where

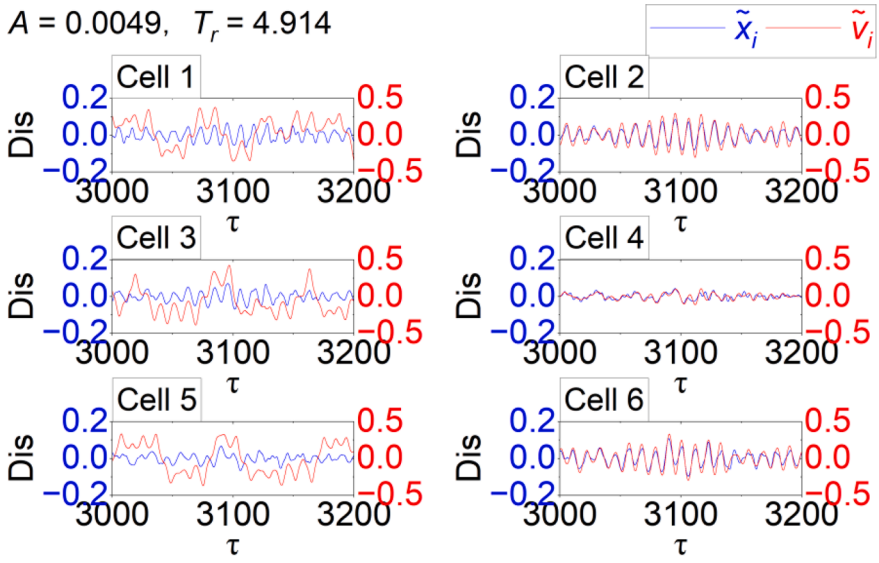

(c)

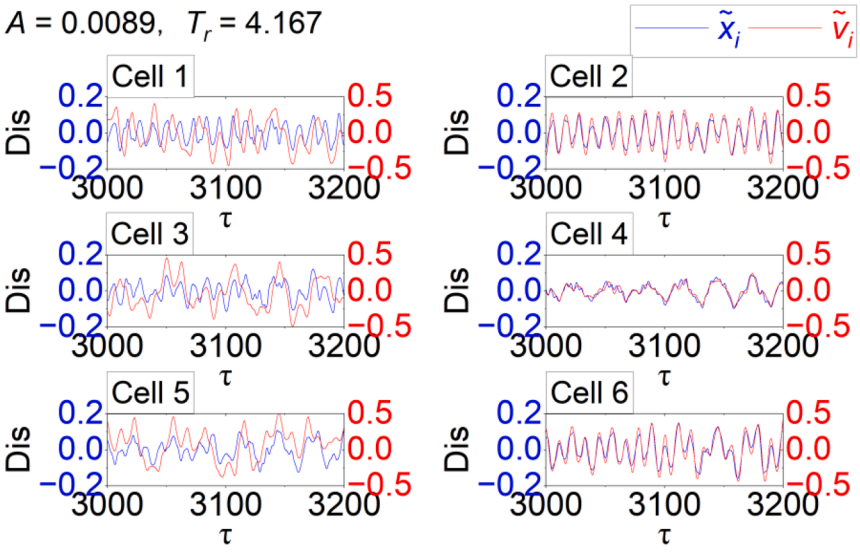

(d)

Fig. 10. (*continued*).

the bandgap is narrowed at low-to-medium accelerations or completely eliminated by the chaotic oscillations at high accelerations [21]. In terms of energy harvesting, broad nonlinear power output bandwidth is obtained as shown in Fig. 7. The higher the base acceleration, the broader the power output bandwidth. As can be seen in Figs. 6 and 7, the analytical solution matches very well with the numerical simulation, which accurately predicts the bandgap location, the amplitudes of the periodic steady-state oscillation and power output responses, as well as the overall trend of the nonlinear dynamic behavior. Moreover, it effectively predicts the frequency range with the occurrence of chaotic oscillations.

For the graded metastructure case, ω_i is set to follow the pattern of $\omega_i = \omega_1(1+\Delta)^{i-1}$, where Δ is the linearized natural frequency spacing index. The locally resonant bandgap size of a metastructure chain is roughly $\omega_i(\sqrt{1+\mu}-1)$, implying that the bandgap size increases with increasing ω_i. With the selected exponential variation pattern of ω_i, it is anticipated to obtain a continuously merged wide bandgap for further enhanced vibration suppression. As shown in Fig. 8, the graded nonlinear mestastructure not only effectively attenuates the undesirable resonance peaks outside the bandbap, but also generates a considerably enlarged merged bandgap compared to a uniform linear metastructure. The power output bandwidth is also further broadened, as shown in Fig. 9, as compared to

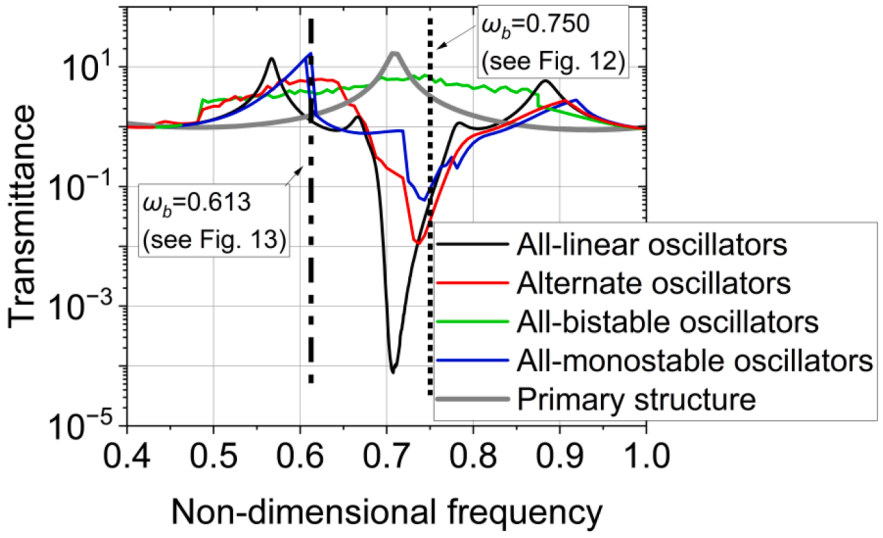

Fig. 11. Comparison of theoretical transmittance responses at $A = 0.0089$ for different nonlinear configurations.

the uniform case in Fig. 7. Again, very well agreement is observed between the analytical solution and the numerical simulation. The location of merged bandgaps, the power output amplitudes as well as the frequency boundaries for the chaotic oscillations to manifest and disappear are all accurately predicted by the analytical solution.

4. Dynamics of the nonlinear metastructure

This section further investigates the dynamic behaviours of the proposed nonlinear metastructure, focusing on the uniform configuration. Fig. 10 shows the numerical time-domain absolute displacements for M_0 and M_1 (i.e., $\hat{x}_i$ and $\hat{v}_i$) in each cell at different levels of base acceleration A. The system parameters are the same as those given in Table 2. The excitation frequency is $\omega_b = 0.569$, which is around the left resonance peak outside the bandgap (refer to the dash line in Fig. 6). At a low acceleration of $A = 0.0005$ (Fig. 10(a)), both the monostable cubic-hardening resonators in Cell 2, 4, and 6 and the bistable resonators in Cell 1, 3 and 5 undergo periodic oscillation, where the bistable ones remain confined within one of the potential wells. At higher $A = 0.0020$, 0.0049 and 0.0089 (Fig. 10(b-d)), the bistable resonators exhibit inter-well chaotic oscillations, which gradually intensify with the increase of A. Consequently, the monostable cubic-hardening resonators as well as the primary structure are also induced to oscillate chaotically. However, a closer examination of the phase differences between the bistable resonators and the primary structure (left columns in Fig. 10(a-d)) reveals that the initially in-phase oscillations at low acceleration intermittently become out-of-phase at higher accelerations as the bistable oscillator jumps from one potential well to the other. In contrast, the monostable resonators consistently undergo in-phase oscillations with the primary structure. Therefore, it is reasonable to deduce that the implementation of bistable resonators contributes to the attenuation of the unwanted resonance peaks due to their inter-well chaotic oscillations. However, further investigation demonstrates that relying solely on bistable resonators in the metastructure is not the optimal choice.

As shown in Fig. 11, at a high acceleration of $A = 0.0089$, the transmission bandgap completely disappears in the metastructure comprising solely bistable resonators. To emphasize the necessity of combining the monostable and bistable mechanisms, Fig. 12 compares the time domain displacement responses of the proposed metastructure with the all-bistable counterpart at $\omega_b = 0.75$ within the linear transmission bandgap (indicated by the dotted line in Fig. 11). The phase portraits with Poincaré points of the local resonator in each cell are also given. In the all-bistable metastructure, chaotic inter-well oscillations do not occur at $A = 0.0005$, as shown in Fig. 12(c), but they are present at a higher $A = 0.0089$ in all the resonators, as illustrated in Fig. 12(g). The phenomenon can also be observed in the phase portraits. As shown in Fig. 12(d), at the low acceleration level of $A = 0.0005$, the responses in all the local resonators are single periodic and vibration as intra-well oscillations. With elevated acceleration level of $A = 0.0089$, as shown in Fig. 12(h), all the oscillators vibrate as non-periodic interwell-chaotic oscillations. In contrast, in the proposed metastructure, at the same high level of $A = 0.0089$, out-of-phase vibrations are sustained between the resonators and the primary structure, as illustrated in Fig. 12(e), which suggests that the presence of the monostable resonators suppresses the emergence of chaotic oscillations, successfully maintaining the bandgap for efficient vibration suppression. The phase portraits still show single-periodic oscillations for all local resonators, as shown in Fig. 12(f).

On the other hand, relying solely on monostable resonators is not an optimal choice either. As shown in Fig. 11, the metastructure with entirely monostable cubic-hardening resonators fails to attenuate the left resonance peak outside the bandgap, and notably, the peak transmittance is even higher than that of the conventional linear metastructure. Fig. 13 compares the time-domain displacement responses and phase portraits with Poincaré points of the local resonator in each cell of the proposed metastructure with those from the all monostable counterpart at $\omega_b = 0.613$ around the left resonance (indicated by dash-dot line in Fig. 13). In the all-monostable case,

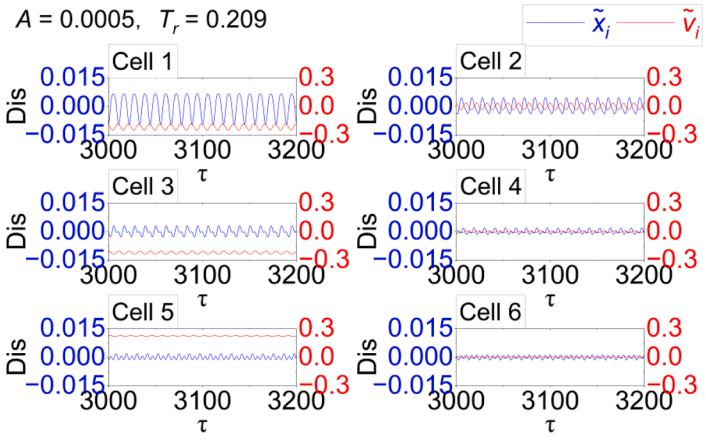

(a)

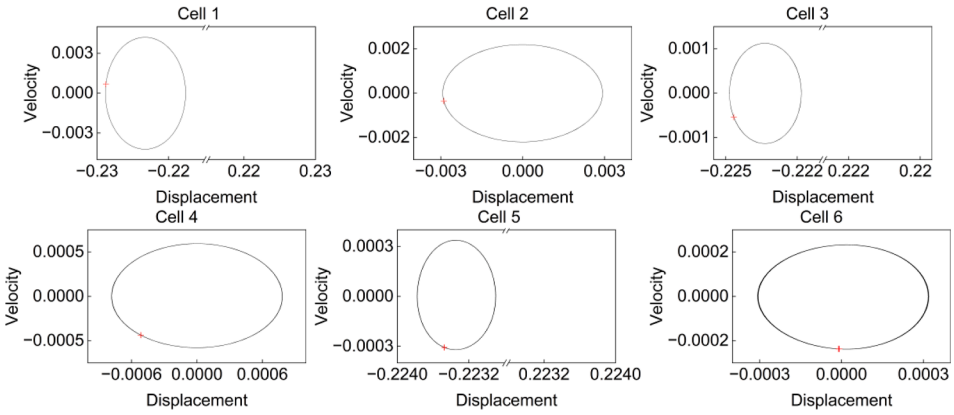

(b)

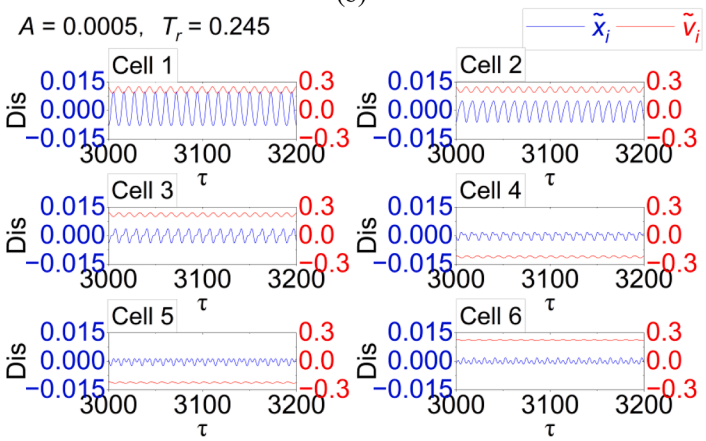

(c)

Fig. 12. Numerical time domain response of the primary structure (blue) and the local resonator (red) of each cell (a, c, e and f) and phase portrait with Poincaré points of the local resonator in each cell (b, d, f and h) at $\omega_b = 0.75$. At $A = 0.0005$: (a-b) alternate configuration, (c-d) all-bistable configuration; at $A = 0.0089$: (e-f) alternate configuration, (g-h) all-bistable configuration. (For interpretation of the references to colour in this figure legend, the reader is referred to the web version of this article.)

the primary masses and the resonators consistently undergo in-phase oscillations in all cells, amplifying the primary structure's oscillation. In the phase portraits, as shown in Fig. 13(d), single periodic oscillations can be observed, with a fractional frequency component modulating the response. The Poincaré points are located within a small range. However, it is evident that the chaotic oscillations in the bistable cells of the proposed design suppress such in-phase oscillation in the monostable cells, with more discretized

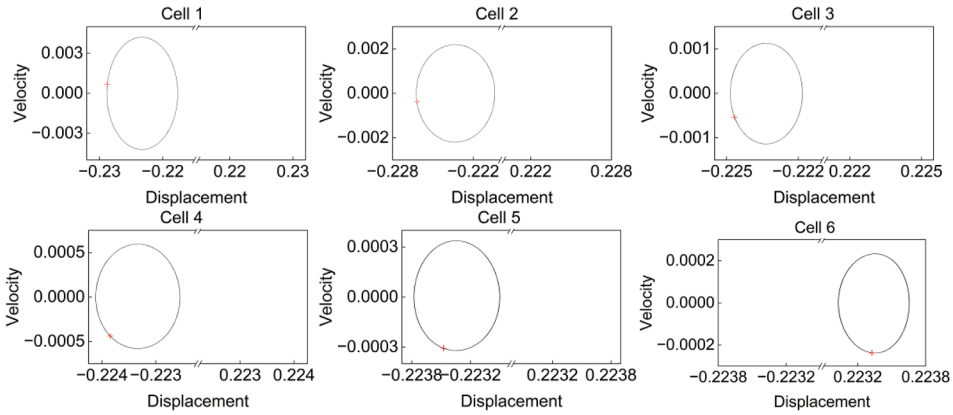

(d)

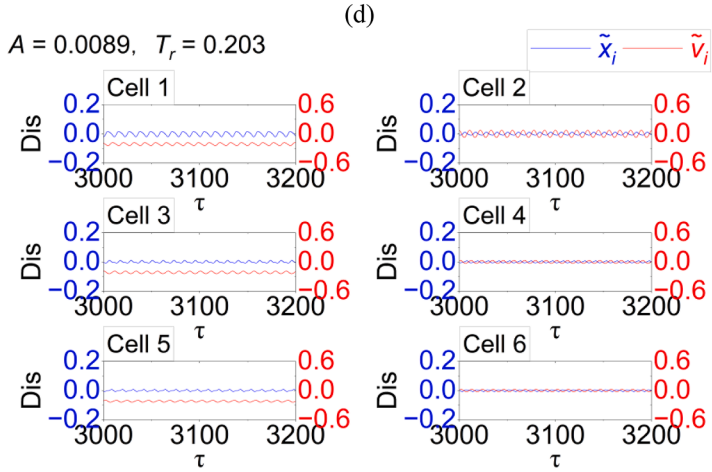

(e)

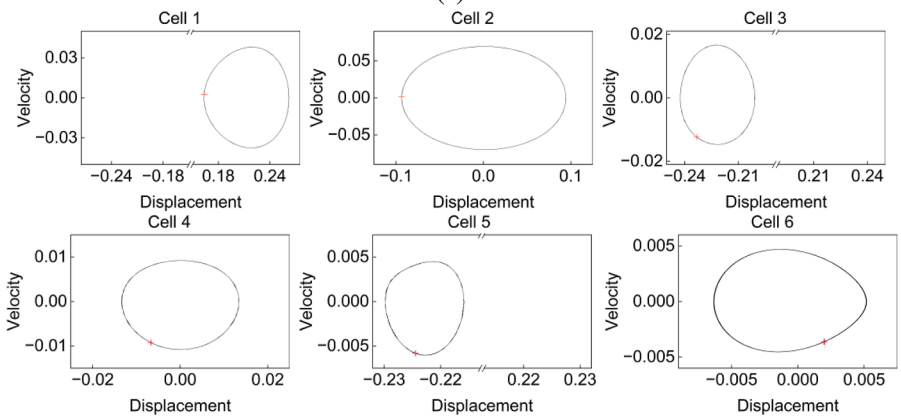

(f)

Fig. 12. (*continued*).

dots in the Poincaré map even in the non-bistable local resonators, as shown in Fig. 13(b), ultimately leading to an effective attenuation of the unwanted resonance.

A comparison of the bandgap size and maximum transmittance is further conducted for the all-bistable, all-monostable, and the proposed configuration in Fig. 14, where the load resistance r_L is no longer kept constant but instead set to the optimal load resistance r_{Lopt} specific to each frequency. Here we define r_{Lopt} as the one that yields the highest total power output combinedly from all resonator harvesters (all resonators are with identical r_L) at each frequency. As can be seen in Fig. 14 (a), for the uniform case at low accelerations, the bandgap sizes of the three configurations are comparable. As the acceleration increases, the bandgap sizes of the all-monostable as well as the proposed configuration generally remain unchanged; in contrast, the all-bistable configuration

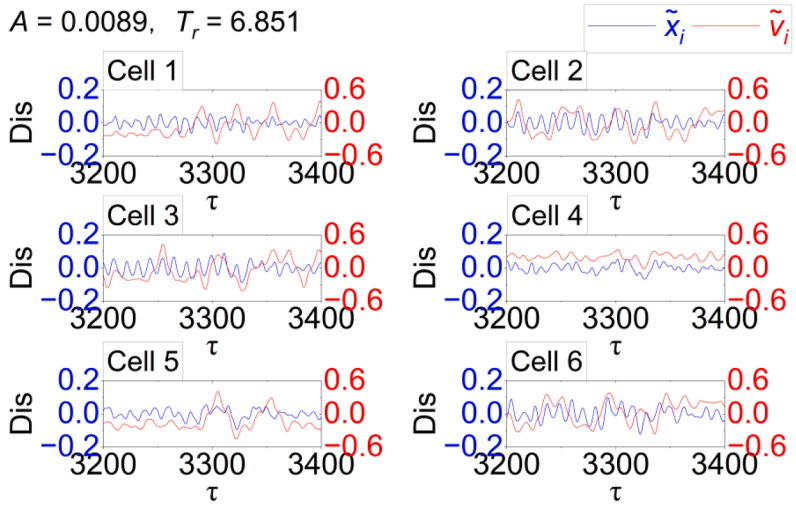

(g)

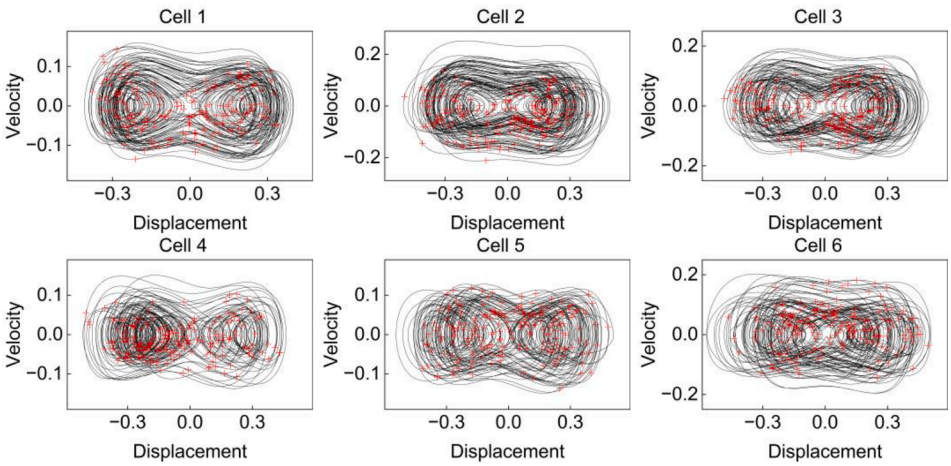

(h)

Fig. 12. (*continued*).

experiences a dramatic reduction in the bandgap size, eventually reaching zero. In the graded case, the decreasing trend is even more pronounced for the all-bistable configuration; while although the bandgap size for the proposed configuration also slightly decreases with increasing acceleration, it remains much larger than that of the all-bistable one at high acceleration. Regarding the maximum transmittance which occurs around the two resonance peaks outside the bandgap, Fig. 14(b) demonstrates that it is not significantly affected by the acceleration. Despite its ability to maintain the bandgap, the all-monostable case always yields the highest transmittance, surpassing even the conventional linear metastructure, undermining the vibration suppression function. Again, it is evident that the proposed metastructure is able to achieve a well-balanced performance by attenuating the unwanted resonance peaks while maintaining a sufficiently large transmission bandgap.

5. Parametric analysis

5.1. Influence of cubic stiffness k_3

Fig. 15 investigates the influence of the cubic stiffness k_3 of the nonlinear resonators on the vibration suppression performance of the proposed metastructure, specifically at a relatively high acceleration $A = 0.0089$. In the figure, k_{3b} represents the cubic stiffness in the bistable resonators (i.e., Cell 1, 3, 5), while k_{3m} represents the cubic stiffness in the monostable cubic-hardening resonators (i.e., Cell 2, 4 and 6).

Fig. 15(a) demonstrates that with small k_{3b} (e.g., $k_{3b} = 0.01$), the proposed nonlinear metastructure behaves similarly to a conventional linear one, where the ability to suppress the unwanted resonance peaks outside the bandgap is lost. On the other hand, with large k_{3b} (e.g., $k_{3b} = 5$ and 10), the transmittance is amplified around the resonance peaks. This can be attributed to the fact that as k_{3b}

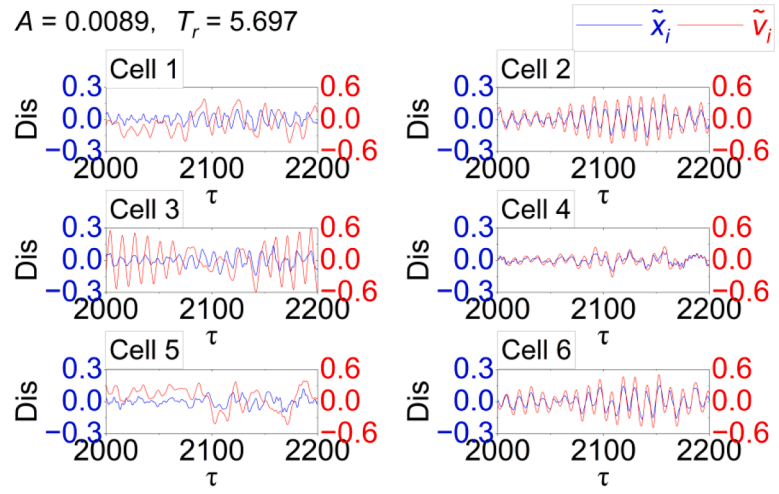
A = 0.0089, T_r = 5.697
x̃_i
ṽ_i
Cell 1
Cell 2
Cell 3
Cell 4
Cell 5
Cell 6
Dis
τ

(a)

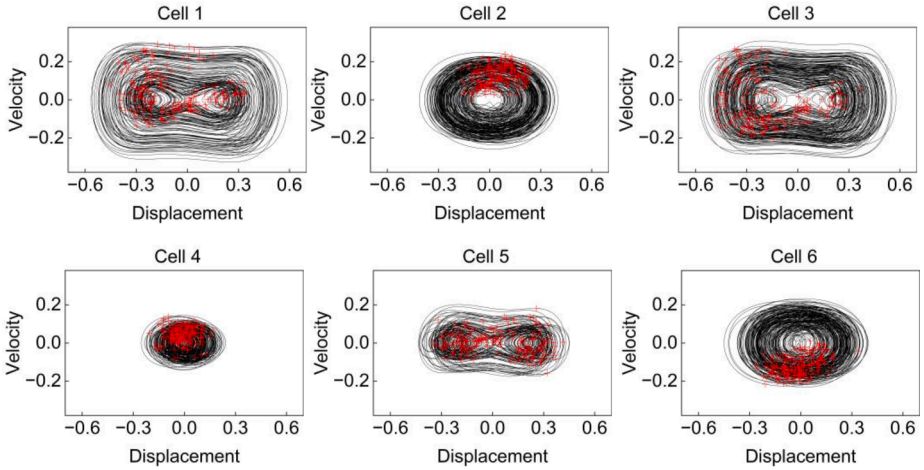
Cell 1
Cell 2
Cell 3
Cell 4
Cell 5
Cell 6
Velocity
Displacement

(b)

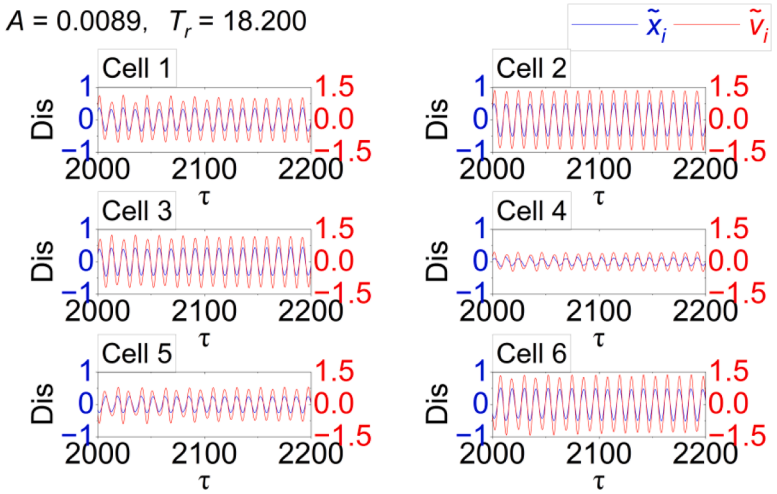
A = 0.0089, T_r = 18.200
x̃_i
ṽ_i
Cell 1
Cell 2
Cell 3
Cell 4
Cell 5
Cell 6
Dis
τ

(c)

Fig. 13. Numerical time domain response of the primary structure (blue) and the local resonator (red) of each cell (a and c) and phase portrait with Poincaré points of the local resonator in each cell (b and d) at $\omega_b = 0.613$. At $A = 0.0089$: (a-b) alternate configuration, (c-d) all-monostable-cubic hardening configuration. (For interpretation of the references to colour in this figure legend, the reader is referred to the web version of this article.)

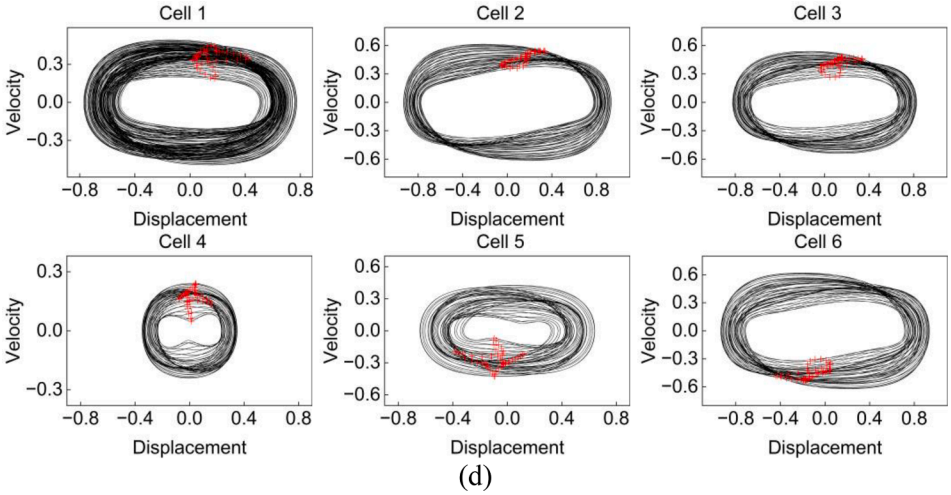

Fig. 13. (*continued*).

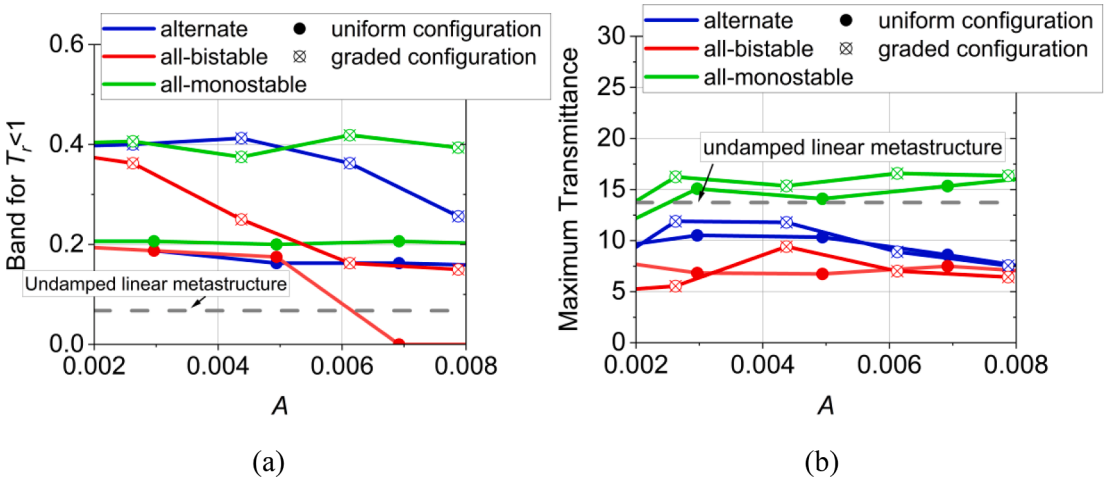

Fig. 14. Comparison of (a) bandgap size and (b) maximum transmittance under various excitation levels for different nonlinear configurations. $\Delta = 0.1$ for all graded configurations.

increases, the two equilibrium positions of the bistable resonator $\pm\sqrt{-k_1/k_{3b}}$ get closer, simultaneously, the height of the barrier between the potential wells decreases, facilitating the entry of the bistable resonator sinto inter-well periodic oscillation around the resonance of the system. Consequently, the transmission attenuation capability that depends on chaotic oscillation ceases to exist. It is worth noting that the bandgap size is significantly reduced with large k_{3b}, as the bistable resonator easily escapes out of the out-of-phase intra-well oscillation. Overall, a medium k_{3b} (e.g., $k_{3b} = 0.1$, 0.5 and 1) is recommended for effective unwanted resonance peak attenuation and bandgap persevation. Regarding k_{3m}, a medium value (e.g., $k_{3m} = 0.5$ and 1) is preferrable. A small k_{3m} (e.g., $k_{3m} = 0.01$ and 0.1) appears to increase the right resonance peak outside the bandgap. With higher k_{3m}, the high-amplitude-resonating response are deviated towards higher frequencies, which gives chance to avoid inter-well chaotic oscillations around the right resonance peak in the bistable local resonators (e.g., Fig. 15(b) around $\omega_b = 0.85$ while $k_{3m} \geq 0.5$ 1). However, a large k_{3m} (e.g., $k_{3m} =$ 5 and 10) tends to eliminate the bandgap.

5.2. *Effect of mass ratio*

Fig. 16 investigates the influence of the mass ratio $\mu = M_1/M_0$ on the vibration attenuation performance of the proposed metastructure, while subjected to a relatively high acceleration level of $A = 0.0089$. As shown in Fig. 16(a), as μ is varied from 0.1 to 0.5, the

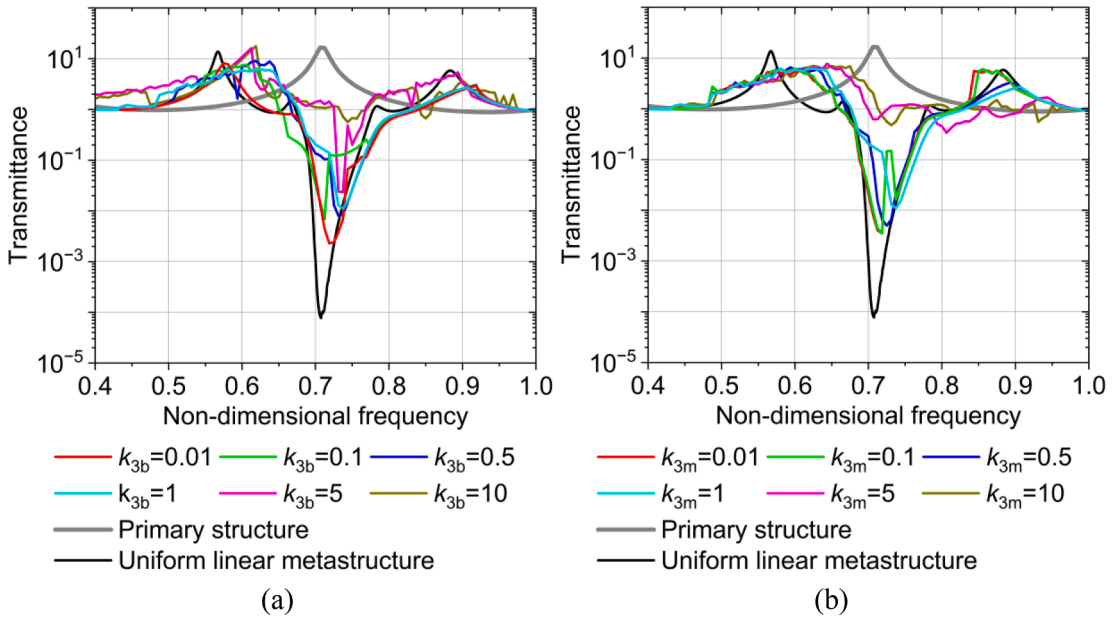

Fig. 15. Comparison of theoretical transmittance responses with different cubic stiffnesses of nonlinear resonators. (a) different k_{3b} and (b) different k_{3m}. $A = 0.0089$.

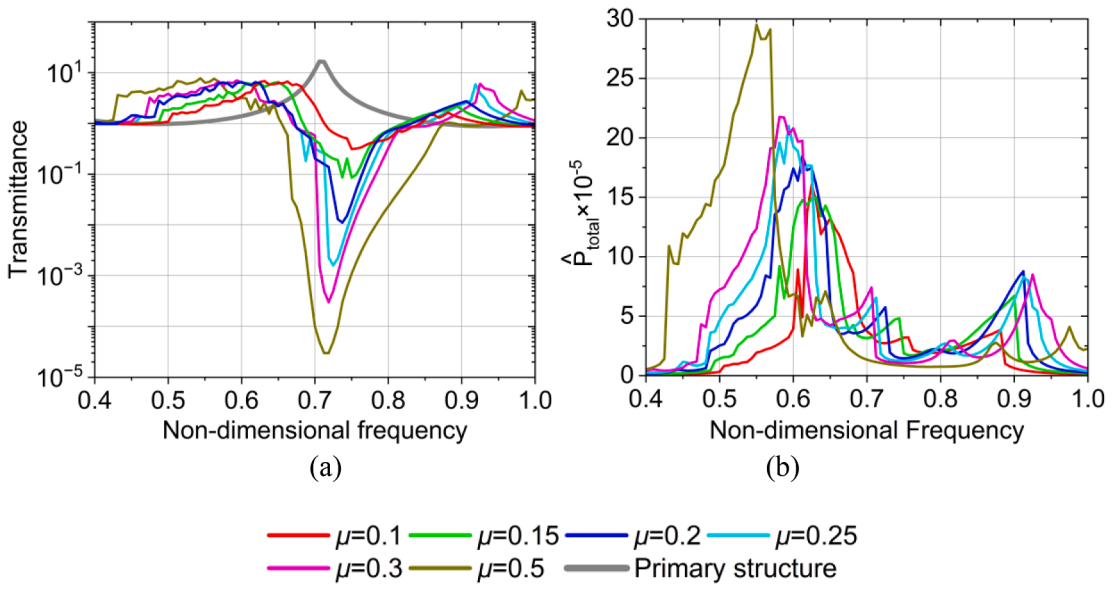

Fig. 16. Comparison of theoretical transmittance responses with different mass ratio. $A = 0.0089$.

bandgap gradually widens; meanwhile, the unwanted resonating peak around $\omega_b = 0.55$ is attenuated for all selected μ values, and the peak around $\omega_b = 0.88$ is deviated to higher frequencies, both benefiting low-frequency vibration attenuation. In terms of power generation, the peak power is increased with increasing μ, however, the power bandwidth is not noticeably affected. In all, larger μ favors both vibration suppression and energy harvesting. Nonetheless, the added mass is usually limited in practical applications where compact designs are required, therefore, selection of μ should consider such practical upper limits.

5.3. *Effect of load resistance and electromechanical coupling*

The influence of the connected load resistance r_L on the performance of the proposed alternate metastructure is investigated in Figs. 17 and 18. A weak electromechanical coupling of $k_e = 0.0056$ is employed in Fig. 17, while a strong coupling of $k_e = 0.0445$ is

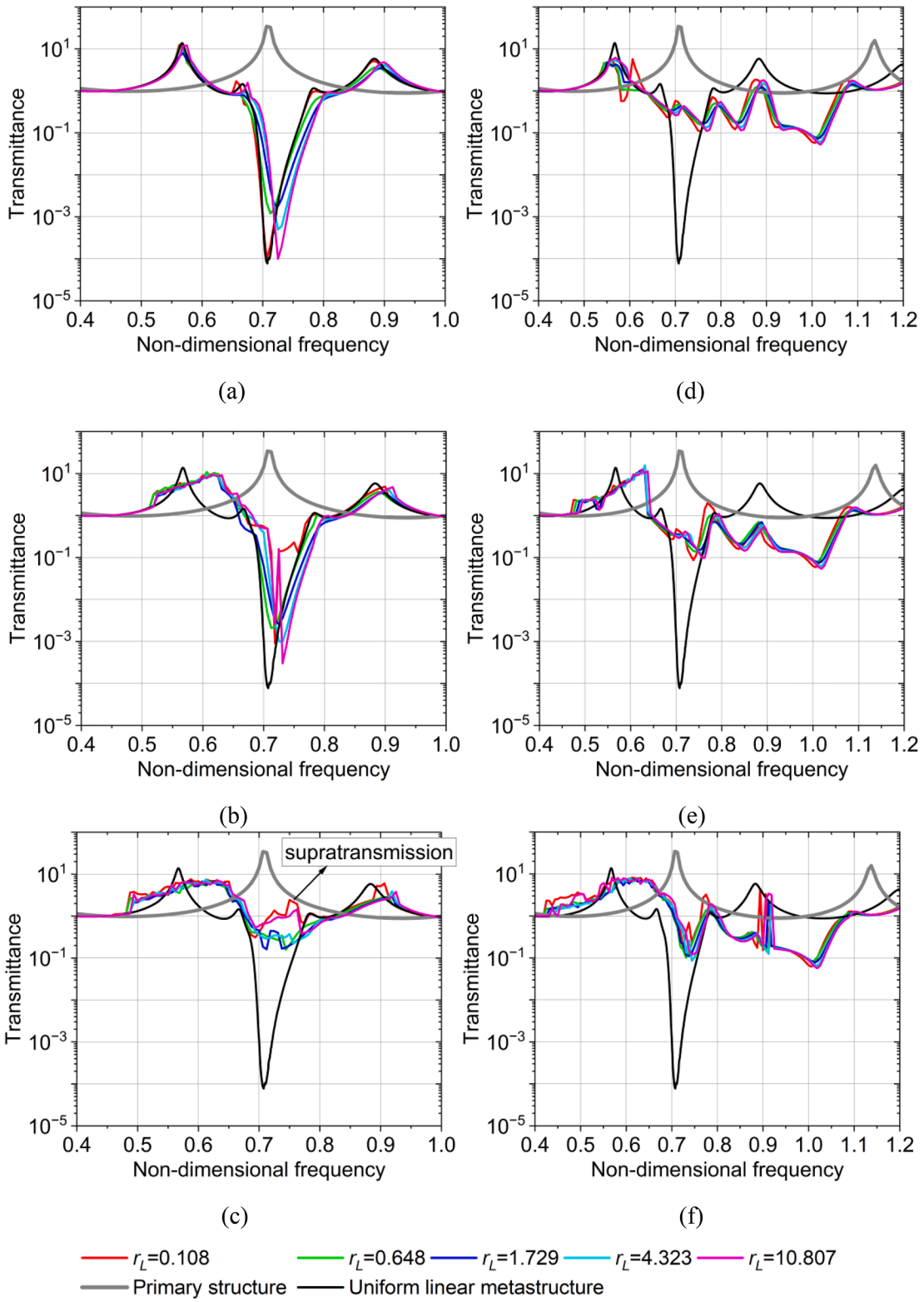

Fig. 17. Comparison of theoretical transmittance responses with different load resistances r_L, with weak coupling $k_e = 0.0056$. Left column: uniform configuration, $A =$ (a) 0.0010, (b) 0.0049 and (c) 0.0089; right column: graded configuration, $\Delta = 0.1$: $A =$ (d) 0.0009, (e) 0.0044 and (f) 0.0079.

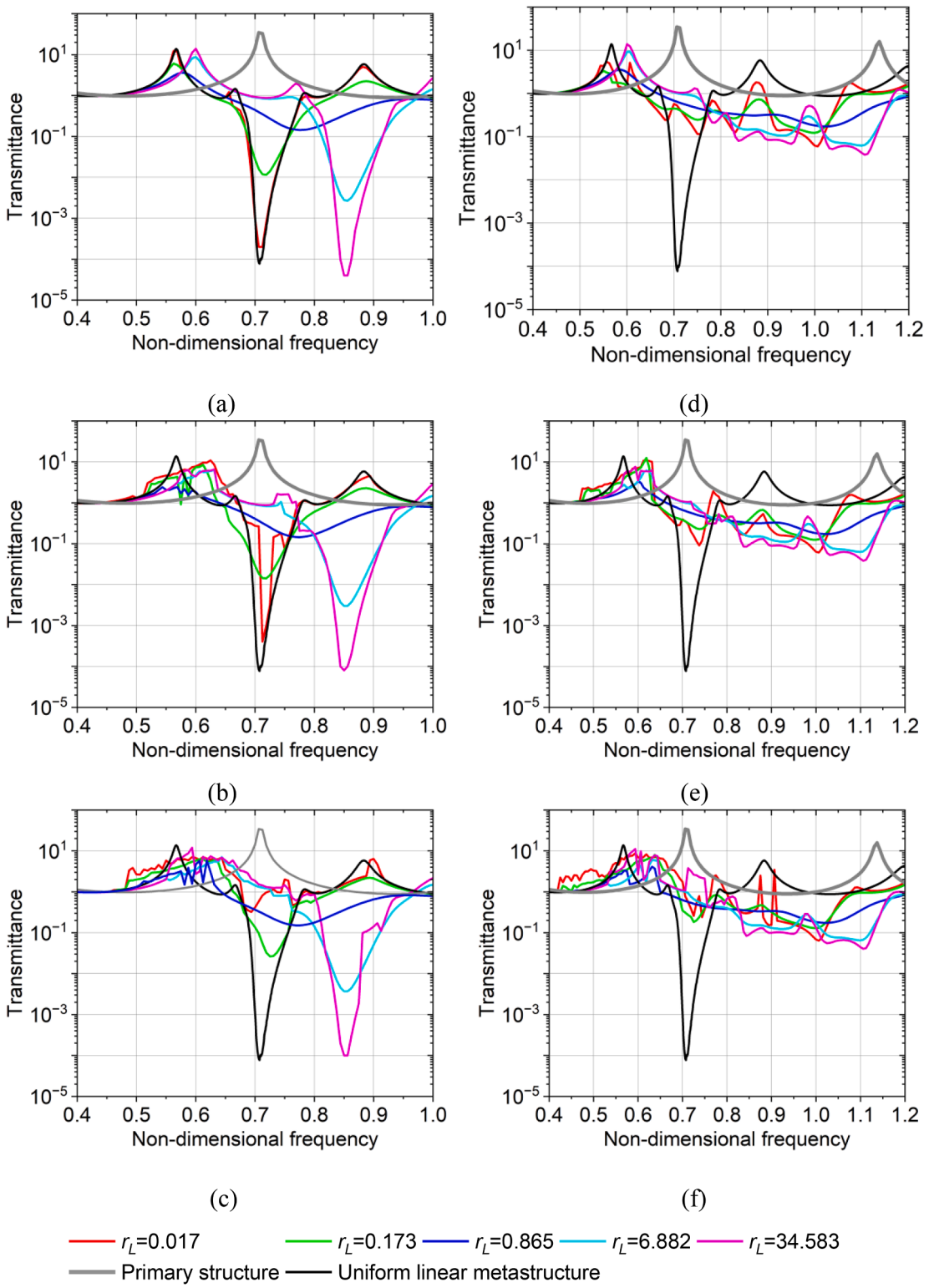

Fig. 18. Comparison of theoretical transmittance responses with different load resistances r_L, with strong coupling $k_e = 0.0445$. Left column: uniform configuration, A = (a) 0.0010, (b) 0.0049 and (c) 0.0089; lower row: right column, $\Delta = 0.1$: A = (d) 0.0009, (e) 0.0044 and (f) 0.0079.

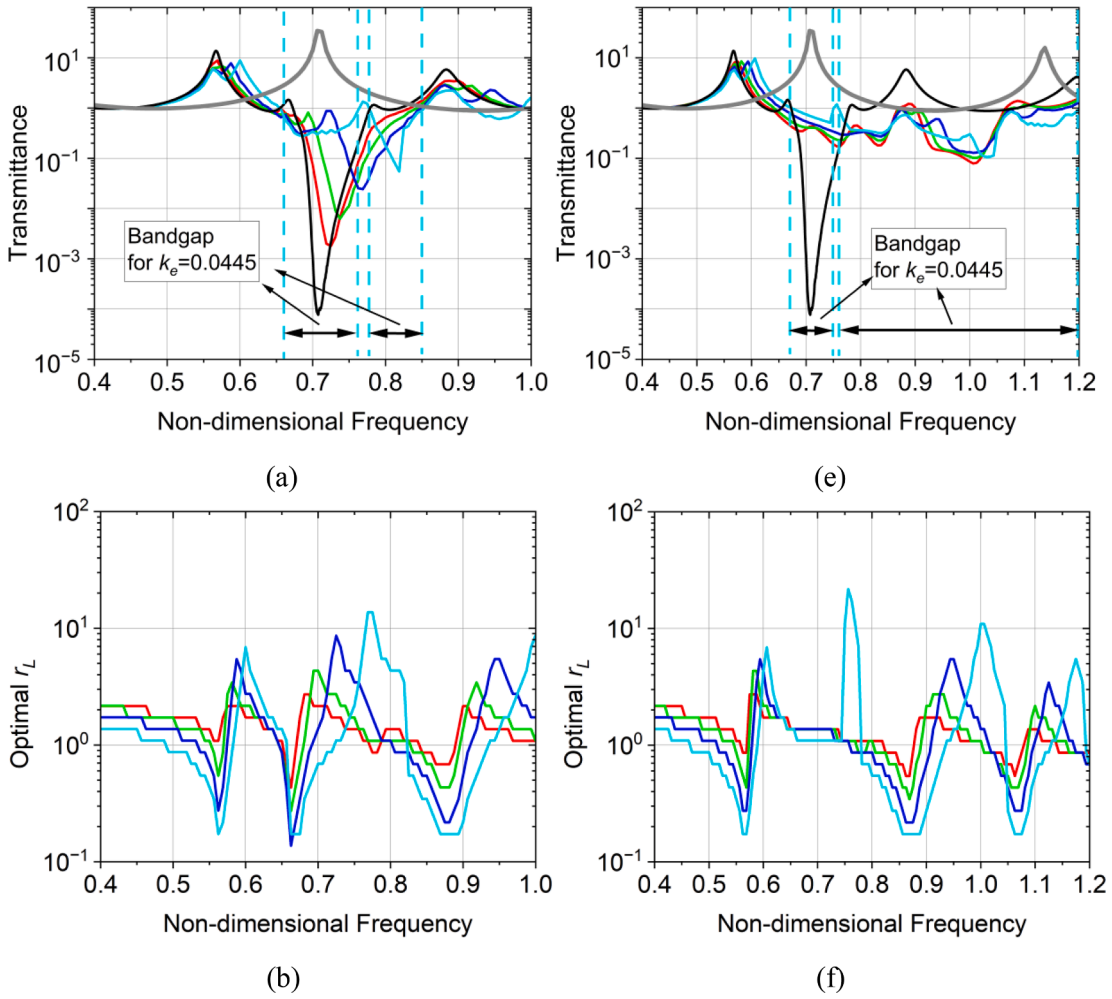

Fig. 19. Comparison of theoretical transmittance responses under different electromechanical coupling strengths k_e. Left column: uniform configuration, A = (a) 0.0010, (c) 0.0049 and (d) 0.0089; right column: graded configuration, $\Delta = 0.1$: A = (d) 0.0009, (g) 0.0044 and (h) 0.0079. Results are obtained at the optimal load resistance r_{Lopt}. Example variation of r_{Lopt}: (b) uniform configuration and (f) graded configuration.

used in Fig. 18. Under the weak coupling condition, as can be seen in Fig. 17, increasing r_L slightly shifts the bandgap to the right, however, it does not obviously affect the overall resonance attenuation capability and bandgap size of the metastructure, which is as expected since the backward electrical damping effect is minimal. It is worth noting that in Fig. 17(c), when the base acceleration is high, utilizing an excessively small or large r_L (i.e., approaching short and open circuit condition, respectively) leads to supra-transmission within the bandgap and reduce the bandgap size, due to the significant reduction in electrical damping.

In contrast, when the electromechanical coupling is strong, Fig. 18 demonstrates that the variation of r_L causes substantial changes in the dynamic response of the system. As r_L increases, the unwanted resonance peaks outside the bandgap initially decrease, reach a minimum, and then increase; meanwhile, the bandgap size initially increases, reaches a maximum, and then decreases. A medium r_L around $r_L = 0.865$ yields the best attenuation of unwanted resonances and the widest bandgap, while other r_L away from this value is not ideal for widening the bandgap in the uniform configuration or achieving a continuous merged bandgap without supratransmission in the graded configuration. To summarize, in terms of vibration attenuation, the weak coupling condition allows for flexible tuning of r_L, whereas the strong coupling condition requires cautious adjustment of r_L to achieve the optimal performance.

Fig. 19 investigates the influence of coupling strength k_e on vibration suppression under variant acceleration levels. To evaluate the effectiveness of vibration suppression under optimal energy harvesting condition, the load resistance is tuned to the optimal load resistance r_{Lopt} that produces the highest power output for each frequency. In the case of uniform configuration (Fig. 19(a-d)), at a low acceleration $A = 0.0010$ as shown in Fig. 19(a), increasing k_e widens the bandgap. Notably, a double-valley bandgap emerges with strong coupling (e.g., $k_e = 0.0223$ and 0.0445). However, the bandgap widening effect becomes less pronounced when the acceleration increases to a medium value of $A = 0.0049$, as seen in Fig. 19(c). At high acceleration $A = 0.0089$ (Fig. 19(d)), increasing k_e tends to narrow down or even eliminate the bandgap. In the graded case (Fig. 19(e-h)), strong coupling slightly broadens the merged bandgap

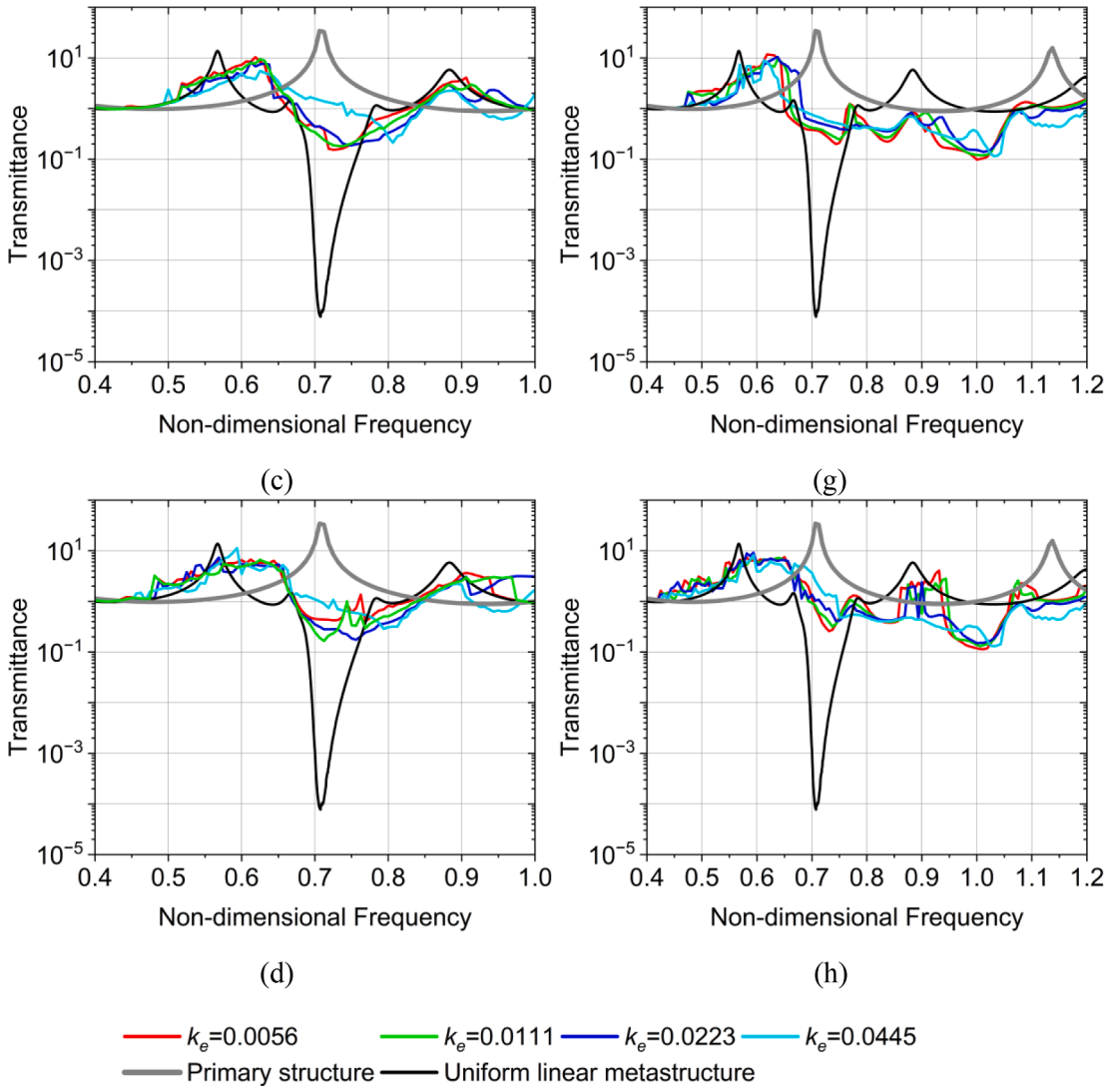

Fig. 19. (*continued*).

at low and medium accelerations, as shown in Fig. 19(e) and 19(g). Furthermore, at high acceleration (Fig. 19(h)), strong coupling can suppress or eliminate the supratransmission within the merged bandgap associated with weak coupling, e.g., between $\omega_b = 0.85$–0.95 with $k_e = 0.0056$, which is beneficial for vibration suppression purposes. The variation of r_{Lopt} is presented in Fig. 19(b) and 19(f) using the low acceleration case as an example. The power seems to be sensitive to r_L at the transmission peaks and valleys, causing sharp shifts in r_{Lopt} at these locations. However, it will be demonstrated later that careful tuning of r_L at each frequency is not necessarily essential, and the sacrifice in power output is minimal. Overall, for the uniform configuration, strong coupling is preferrable at low accelerations, whereas weak coupling is preferrable at high accelerations. In contrast, for the graded configuration, strong coupling is always preferrable.

To assess the power output level and power bandwidth of the proposed metastructure, Fig. 20 depicts the variation of power output under various load resistances and acceleration levels. Two coupling strengths are examined. At weak coupling $k_e = 0.0056$ as illustrated in Fig. 20(a-c), there is an optimal load resistance r_{Lopt} that leads to both the highest power output and widest power bandwidth. The value of r_{Lopt} remains relatively consistent (i.e., between $r_L = 1.729$ and 4.323) over the considered frequency range, thus it is appropriate to use a constant r_{Lopt} across the entire frequency range and various accelerations, allowing for the simplification of the system design. Although slight shifts in r_{Lopt} are observed around the power peaks (corresponding to the shifts denoted by the red curve in Fig. 19(b) and 19(f)), the resulting difference in power level is minimal. At strong coupling $k_e = 0.0445$, conversely, the behaviour is different. At a low acceleration, as shown in Fig. 20(d), two load resistances of $r_L = 0.173$ and $r_L = 6.882$ yield two comparable peaks, which is a typical phenomenon of vibration energy harvesting under strong electromechanical coupling. Increasing the acceleration level, as shown in Fig. 20(e) and Fig. 20(f), the power gradually becomes highest at $r_L = 0.865$, which also gives the widest power bandwidth. Overall, in terms of power generation, with weak coupling, it is safe to use a constant r_{Lopt} to obtain higher

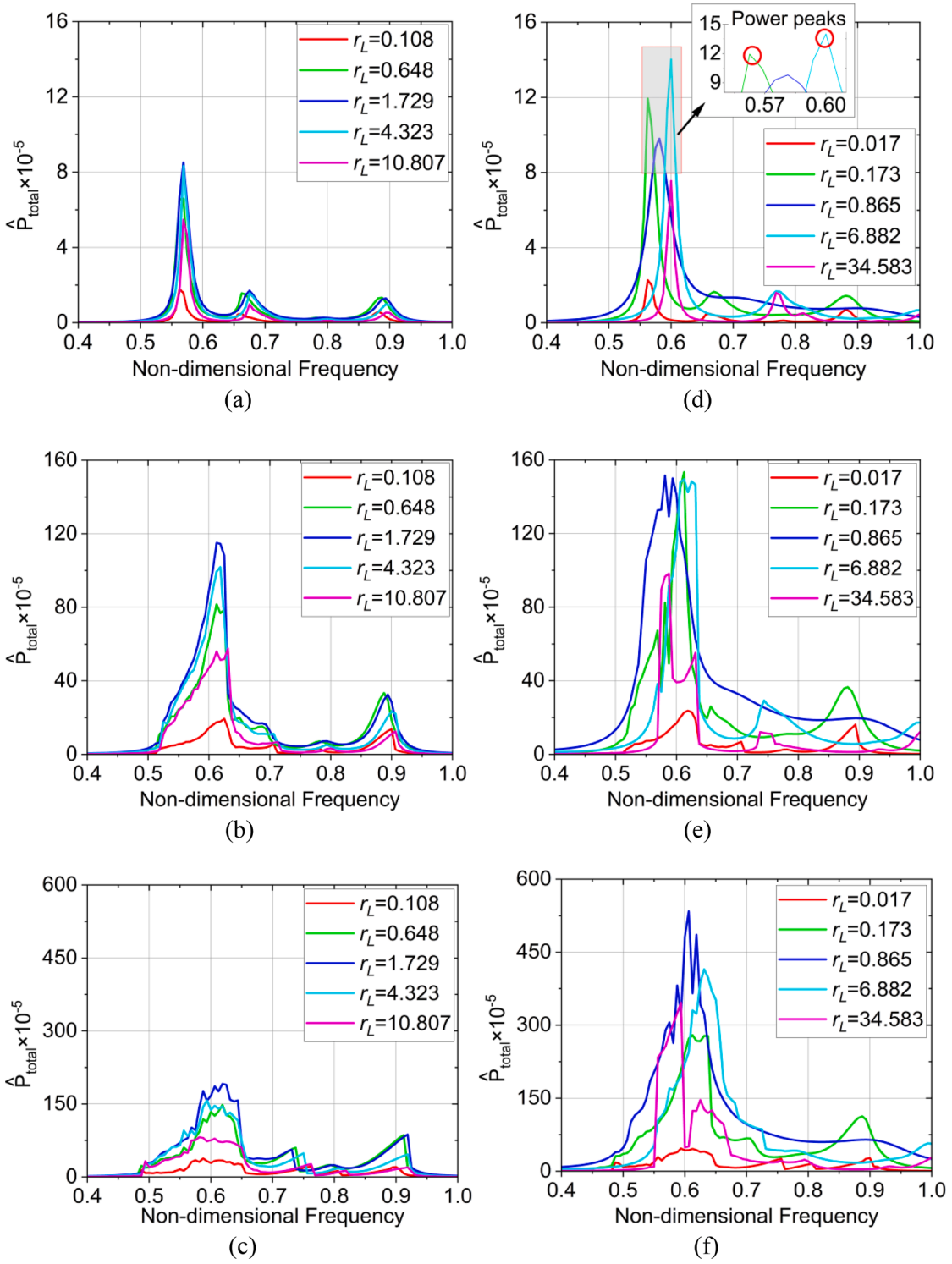

Fig. 20. Comparison of theoretical power output with different load resistances r_L and coupling strengths k_e: (a-c) $k_e = 0.0056$; (d-f) $k_e = 0.0445$. A = (a)(d) 0.0010, (b)(e) 0.0049 and (c)(f) 0.0089.

power level and wider power bandwidth; while with strong coupling, it requires adjustment over a range of r_L to ensure a better performance at different excitation levels.

6. Conclusion

In this paper, a novel dual-functional metastructure for performance-enhanced vibration attenuation and energy harvesting is proposed by utilizing combined bistable and monostable cubic-hardening local resonators that are alternately arranged on a host beam. At a low-frequency range (<20 Hz), the proposed metastructure successfully suppresses the undesired resonance peaks outside the bandgap, achieves a wide bandgap even at high acceleration levels, while generating power over a broad bandwidth. The effectiveness of the proposed metastructure is experimentally evaluated through a fabricated nonlinear prototype and validated through an established distributed-parameter electromechanically coupled model. Experimentally, with a graded configuration, the proposed design suppresses the unwanted resonance peak outside the bandgap by up to 70.5 % while widening the bandgap by 52 %, compared to the linear counterpart. Analytical solutions of the dynamic and electrical response of the proposed structure are explicitly derived based on the harmonic balance method, which accurately predict the nonlinear dynamic behaviours, including the bandgap location, amplitudes of the periodic steady-state oscillation and power outputs. The frequency range with the occurrence of chaotic oscillations can also be effectively predicted. Dynamic analysis shows that outside the bandgap, the implementation of bistable resonators contributes to the attenuation of the unwanted resonance peaks due to their inter-well chaotic oscillations; while within the bandgap, the presence of the monostable resonators suppresses the emergence of chaotic oscillations thus sustaining the out-of-phase vibrations between the resonators and the primary structure.

Design guidelines for the proposed metastructure are provided by examining the influences of the nonlinear stiffness, load resistance, and electromechanical coupling on the mechanical and electrical outputs. It is recommended to apply medium values of cubic nonlinear stiffnesses in both bistable and monostable cubic-hardening oscillators (e.g., $k_{3b} = 0.1$–1 and $k_{3m} = 0.5$–1) to maintain a well-balanced resonance peak attenuation and bandgap preservation. The mass ratio should be either ≤ 0.2 or ≥ 0.5 to achieve good performance for vibration suppression, and higher μ (e.g., $\mu \geq 0.3$) is beneficial for energy harvesting. The weak electromechanical coupling condition allows for simply using a constant load resistance (e.g., $r_L = 1.729$), whereas the strong coupling condition requires cautious adjustment of the load resistance to achieve optimal vibration attenuation and energy harvesting performance. Specifically, a medium r_L around $r_L = 0.865$ yields the best attenuation of unwanted resonances and the widest bandgap. At low excitation level, $r_L = 0.173$ and $r_L = 6.882$ are recommended and when the excitation level is high, a load resistance of $r_L = 0.865$ is recommended to apply to achieve optimal energy harvesting performance. As for the optimal coupling strength, for the uniform configuration, strong coupling (e.g., $k_e \geq 0.0223$) is preferrable at low accelerations, whereas weak coupling (e.g., $k_e \leq 0.0223$) is preferrable at high accelerations. In contrast, for the graded configuration, strong coupling with $k_e \geq 0.0445$ is always preferrable. It is concluded that the proposed design of dual-functional nonlinear metastructure with combined bistable and monostable cubic-hardening local resonators is a viable solution for well-balanced amplitude-robust simultaneous vibration attenuation and energy harvesting.

CRediT authorship contribution statement

Che Xu: Conceptualization, Data curation, Formal analysis, Investigation, Writing – original draft. **Yaowen Yang:** Resources, Supervision, Writing – review & editing. **Chun H. Wang:** Resources, Supervision, Writing – review & editing. **Liya Zhao:** Conceptualization, Formal analysis, Funding acquisition, Investigation, Methodology, Project administration, Resources, Supervision, Validation, Writing – review & editing.

Declaration of competing interest

The authors declare that they have no known competing financial interests or personal relationships that could have appeared to influence the work reported in this paper.

Data availability

Data will be made available on request.

Acknowledgments

We would like to acknowledge the financial support of the Australian Research Council under Grant No. DE210101382.

References

[1] Z. Liu, X. Zhang, Y. Mao, Y. Zhu, Z. Yang, C.T. Chan, P. Sheng, Locally resonant sonic materials, Science 289 (5485) (2000) 1734–1736.
[2] C. Sugino, Y. Xia, S. Leadenham, M. Ruzzene, A. Erturk, A general theory for bandgap estimation in locally resonant metastructures, J. Sound Vib. 406 (2017) 104–123.
[3] J.D. Hobeck, D.J. Inman, *Simultaneous passive broadband vibration suppression and energy harvesting with multifunctional metastructures*, in *Proc. SPIE 10172, A Tribute Conference Honoring Daniel Inman*. 2017. p. 101720K.
[4] Y. Chen, G. Hu, G. Huang, A hybrid elastic metamaterial with negative mass density and tunable bending stiffness, J. Mech. Phys. Solids 105 (2017) 179–198.
[5] K. Wang, J. Zhou, H. Ouyang, L. Cheng, D. Xu, A semi-active metamaterial beam with electromagnetic quasi-zero-stiffness resonators for ultralow-frequency band gap tuning, Int. J. Mech. Sci. 176 (2020).
[6] S.H. Chavan, S.S. Malladi, V.V.N.S. Malladi, Reinforcement Learning approach of switching bi-stable oscillators to adapt bandgaps of 1D-meta-structures, Mech. Syst. Sig. Process. 191 (2023).

[7] P. Wang, F. Casadei, S. Shan, J.C. Weaver, K. Bertoldi, Harnessing buckling to design tunable locally resonant acoustic metamaterials, Phys Rev Lett 113 (1) (2014) 014301.
[8] C. Nimmagadda, K.H. Matlack, Thermally tunable band gaps in architected metamaterial structures, J. Sound Vib. 439 (2019) 29–42.
[9] M. Alshaqaq, A. Erturk, Graded multifunctional piezoelectric metastructures for wideband vibration attenuation and energy harvesting, Smart Mater. Struct. 30 (1) (2021).
[10] G. Hu, A.C.M. Austin, V. Sorokin, L. Tang, Metamaterial beam with graded local resonators for broadband vibration suppression, Mech. Syst. Sig. Process. 146 (2021).
[11] Y. Xiao, J. Wen, X. Wen, Broadband locally resonant beams containing multiple periodic arrays of attached resonators, Phys. Lett. A 376 (16) (2012) 1384–1390.
[12] M. Zhang, J. Yang, R. Zhu, Origami-based bistable metastructures for low-frequency vibration control, J. Appl. Mech. 88 (5) (2021).
[13] Z. Wu, W. Liu, F. Li, C. Zhang, Band-gap property of a novel elastic metamaterial beam with X-shaped local resonators, Mech. Syst. Sig. Process. 134 (2019).
[14] G. Hu, L. Tang, R. Das, Internally coupled metamaterial beam for simultaneous vibration suppression and low frequency energy harvesting, J. Appl. Phys. 123 (5) (2018).
[15] C. Cai, J. Zhou, K. Wang, D. Xu, G. Wen, Metamaterial plate with compliant quasi-zero-stiffness resonators for ultra-low-frequency band gap, J. Sound Vib. 540 (2022).
[16] C. Cai, J. Zhou, K. Wang, Q. Lin, D. Xu, G. Wen, Quasi-zero-stiffness metamaterial pipe for low-frequency wave attenuation, Eng. Struct. 279 (2023).
[17] L. Xiao, O.S. Bursi, H. Li, M. Wang, X.-L. Du, Energy dissipation enhancement of flexural metamaterial beams with inerter and rotational deformation, Int. J. Mech. Sci. 237 (2023).
[18] F. Jamil, F. Chen, B. Deng, R.G. Parker, P. Wang, Inerter-based elastic metamaterials for band gap at extremely low frequency, Extreme Mech. Lett. 56 (2022).
[19] A. Aladwani, A. Mohammed, M. Nouh, Tunable dissipation in elastic metamaterials via methodic reconfiguration of inertant mechanical networks, Meccanica 57 (6) (2022) 1337–1352.
[20] J.A. Mosquera-Sánchez, C. De Marqui, Dynamics and wave propagation in nonlinear piezoelectric metastructures, Nonlinear Dyn. 105 (4) (2021) 2995–3023.
[21] Y. Xia, M. Ruzzene, A. Erturk, Dramatic bandwidth enhancement in nonlinear metastructures via bistable attachments, Appl. Phys. Lett. 114 (9) (2019).
[22] Y. Xia, M. Ruzzene, A. Erturk, Bistable attachments for wideband nonlinear vibration attenuation in a metamaterial beam, Nonlinear Dyn. 102 (3) (2020) 1285–1296.
[23] A. Banerjee, E.P. Calius, R. Das, An impact based mass-in-mass unit as a building block of wideband nonlinear resonating metamaterial, Int. J. Non Linear Mech. 101 (2018) 8–15.
[24] A. Casalotti, S. El-Borgi, W. Lacarbonara, Metamaterial beam with embedded nonlinear vibration absorbers, Int. J. Non Linear Mech. 98 (2018) 32–42.
[25] D.P. Vasconcellos, M. Silveira, Optimization of axial vibration attenuation of periodic structure with nonlinear stiffness without addition of mass, J. Vib. Acoust. 142 (6) (2020).
[26] T. Tan, Z. Yan, H. Zou, K. Ma, F. Liu, L. Zhao, Z. Peng, W. Zhang, Renewable energy harvesting and absorbing via multi-scale metamaterial systems for Internet of things, Appl. Energy 254 (2019).
[27] K. Mikoshiba, J.M. Manimala, C.T. Sun, Energy harvesting using an array of multifunctional resonators, J. Intell. Mater. Syst. Struct. 24 (2) (2012) 168–179.
[28] M. Bukhari, O. Barry, Simultaneous energy harvesting and vibration control in a nonlinear metastructure: a spectro-spatial analysis, J. Sound Vib. 473 (2020).
[29] A. Chaurha, P.V. Malaji, T. Mukhopadhyay, Dual functionality of vibration attenuation and energy harvesting: effect of gradation on non-linear multi-resonator metastructures, Eur. Phys. J. Special Topics (2022).
[30] D.P. Vasconcellos, R.S. Cruz, J.C.M. Fernandes, M. Silveira, Vibration attenuation and energy harvesting in metastructures with nonlinear absorbers conserving mass and strain energy, Eur. Phys. J. Special Topics (2022).
[31] G. Hu, L. Tang, R. Das, Metamaterial-inspired piezoelectric system with dual functionalities: energy harvesting and vibration suppression. *Active and Passive Smart Structures and Integrated Systems*, 2017. 2017..
[32] C. Sugino, A. Erturk, Analysis of multifunctional piezoelectric metastructures for low-frequency bandgap formation and energy harvesting, J. Phys. D Appl. Phys. 51 (21) (2018).
[33] G. Hu, L. Tang, A. Banerjee, R. Das, Metastructure with piezoelectric element for simultaneous vibration suppression and energy harvesting, J. Vib. Acoust. 139 (1) (2017).
[34] L. Zhao, Y. Yang, Enhanced aeroelastic energy harvesting with a beam stiffener, Smart Mater. Struct. 24 (3) (2015).
[35] M.F. Daqaq, R. Masana, A. Erturk, D. Dane Quinn, On the role of nonlinearities in vibratory energy harvesting: a critical review and discussion, Appl. Mech. Rev. 66 (4) (2014).
[36] S.C. Stanton, C.C. McGehee, B.P. Mann, Nonlinear dynamics for broadband energy harvesting: Investigation of a bistable piezoelectric inertial generator, Physica D 239 (10) (2010) 640–653.
[37] A. Ibrahim, S. Towfighian, M.I. Younis, Dynamics of transition regime in bistable vibration energy harvesters, J. Vib. Acoust. 139 (5) (2017).
[38] W. Yang, S. Towfighian, A parametric resonator with low threshold excitation for vibration energy harvesting, J. Sound Vib. 446 (2019) 129–143.
[39] C. Xu, S. Chen, C.H. Wang, Y. Yang, L. Zhao, Amplitude-robust metastructure with combined bistable and monostable mechanisms for simultaneously enhanced vibration suppression and energy harvesting, Appl. Phys. Lett. 122 (15) (2023).
[40] W. Weaver Jr., S.P. Timoshenko, D.H. Young, Vibration Problems in Engineering, John Wiley & Sons, 1991.
[41] C. Sugino, S. Leadenham, M. Ruzzene, A. Erturk, On the mechanism of bandgap formation in locally resonant finite elastic metamaterials, J. Appl. Phys. 120 (13) (2016).
[42] *Hadamard product (matrices)*. Available from: https://en.wikipedia.org/wiki/Hadamard_product_(matrices).